On the use of Advanced Microwave Sounding Unit-A and -B measurements for studying the monsoon variability over West Africa

Laurence Eymard, Fatima Karbou, Serge Janicot, Nadine Chouaib, Françoise Pinsard

HAL Id: hal-00952742

https://hal.sorbonne-universite.fr/hal-00952742v1

Submitted on 27 Feb 2014

On the use of Advanced Microwave Sounding Unit-A and -B measurements for studying the monsoon variability over West Africa

Laurence Eymard,[1] F. Karbou,[2,3] S. Janicot,[1] N. Chouaib,[1] and F. Pinsard[1]

[1] The advanced microwave sounding unit (AMSU) -A and -B sensors provide observations of humidity and temperature that are relevant for meteorological and climate studies. The use of these observations in numerical weather prediction models has increased in the past 10 years because of some improvements in data assimilation. However, an appropriate use of AMSU measurements apart from assimilation context is rather difficult and depends for the most part on how successfully the instrumental characteristics are accounted for. In particular, atmosphere humidity and temperature variations can be completely hidden by features because of the effect of the observation zenith angle. In this paper, 8 years of AMSU-A and -B observations have been corrected from the observations zenith angle effect and have been used to study temperature and humidity variations over West Africa. Comparisons have been made between AMSU observations and selected atmospheric fields from European Centre for Medium-Range Weather Forecasts analyses as well as outgoing longwave radiation estimates. It has been found that observations from AMSU-A channel 5 can be used to monitor the heat low evolution and that AMSU-B observations from channels 3 and 5 are well adapted to study the humidity variations in direct link with the African monsoon from intraseasonal to interannual scales.

1. Introduction

[2] Advanced microwave sounding unit-A and -B (AMSU-A and AMSU-B) are two operational instruments predominantly dedicated to measuring temperature and humidity at many levels of the atmosphere. Data from these instruments have been widely used in data assimilation and have been recognized to improve the quality of analyses and forecast skills. The assimilation of these measurements in numerical weather prediction (NWP) models has been substantially improved, but efforts are still needed in order to better use AMSU measurements in nearly every atmospheric and surface condition. In particular, many efforts have been devoted to improve the assimilation of AMSU observations by improving the land surface emissivity description [*Karbou et al.*, 2006, 2010a; *Prigent et al.*, 2005; *Krzeminski et al.*, 2008] and also by improving the

ice sheet emissivity modeling [*Bouchard et al.*, 2010; *Guedj et al.*, 2010]. First assimilation trials using low-level AMSU-B humidity observations over land, which are usually rejected from assimilation systems, have been found very useful in improving the analysis of humidity in the tropics [*Karbou et al.*, 2010b]. The improvement in analyzed humidity has been successfully evaluated over West Africa against independent GPS measurements from the African Monsoon Multidisciplinary Analysis (AMMA) project (see *Bock et al.* [2008] for the GPS network, and *Redelsperger et al.* [2006a, 2006b] for an overview of the AMMA project).

[3] AMMA is an international project aiming to improve our knowledge and understanding of the West African monsoon (WAM) and its variability at different time scales: daily to interannual [*Redelsperger et al.*, 2006a]. However, available NWP analyses or reanalyses of the atmosphere are produced from assimilation systems which have up to now operationally used few low-level temperature and humidity observations over land surfaces. This is critical for areas that are nearly void of in situ measurements and that are paradoxically of primary importance for climate and meteorological studies. For instance, over the tropical/subtropical belt, the lack of meteorological measurement is obvious: few regular ship lines carry radio sounding automatic stations,

[1]LOCEAN, IPSL, CNRS, Paris, France.
[2]Météo-France, Toulouse, France.
[3]CNRM-GAME, CNRS, Toulouse, France.

Table 1. AMSU-A and AMSU-B Channels

Channel Number	Frequency (GHz)	Noise Equivalent (K)	Resolution at Nadir (km)
AMSU-A			
1	23.8	0.30	48
2	31.4	0.30	48
3	50.3	0.40	48
4	52.8	0.25	48
5	53.596 ± 0.115	0.25	48
6	54.4	0.253	48
7	54.9	0.25	48
8	55.5	0.25	48
9	$57.290 = f_0$	0.25	48
10	$f_0 \pm 0.217$	0.40	48
11	$f_0 \pm 0.322 \pm 0.048$	0.40	48
12	$f_0 \pm 0.322 \pm 0.022$	0.60	48
13	$f_0 \pm 0.322 \pm 0.010$	0.80	48
14	$f_0 \pm 0.322 \pm 0.0045$	1.20	48
15	89	0.50	48
AMSU-B			
16	89	0.37	16
17	150	0.84	16
18	183.31 ± 1	1.06	16
19	183.31 ± 3	0.70	16
20	183.31 ± 7	0.60	16

large forest areas and deserts are natural limitations, which are added to economical difficulties in many countries. The major meteorological and climatic variability over West Africa is related to the monsoon, leading to alternation of wet and dry seasons over a wide portion of the continent. Related phenomena are observed over the Gulf of Guinea and the eastern Atlantic (surface changes in wind and surface temperature). The deep convection associated with the summer monsoon is one of the major features of the seasonal and intraseasonal variability [*Sultan and Janicot*, 2003].

[4] For climate studies over areas with a poor in situ network, such as the tropics, it is important either to evaluate the atmospheric analyses using independent measurements or to assimilate more temperature and humidity observations over the region. In the meantime, one can seek for alternatives to better use available observations in parallel to assimilation studies.

[5] This work has the objective to investigate the potential of a direct use of AMSU-A and -B brightness temperatures in the tropics, without assimilation or retrieval techniques, to statistically infer the temperature and humidity variability in the atmosphere. This approach allows one to exploit data in places where assimilation or retrieval are difficult, as is the case for the African monsoon region. To do so, AMSU data have to be processed in order to account for the observation variability along the scan among other effects. The end result is an 8 year AMSU climatology (2000–2007) of several selected temperature and humidity channels. The climatology has been studied in depth and compared with the recently produced ERA-Interim reanalyses from European Centre for Medium-Range Weather Forecasts (ECMWF) [*Simmons et al.*, 2007].

[6] AMSU measurements and their processing are presented in section 2. In section 3, the AMSU-A and AMSU-B brightness temperature climatology is examined and is

compared to ECMWF analyses, and a focus is made on three seasons of the AMMA Enhanced Observing Period (2006).

2. Data and Methods

2.1. AMSU-A and -B Measurements

[7] AMSU-A and AMSU-B (or Microwave Humidity Sounder (MHS)) are two cross-track scanning microwave sensors. It should be noted here that MHS channels are slightly different from AMSU-B channels. AMSU instruments are on board several polar-orbiting satellites such as the National Oceanic and Atmospheric Administration (NOAA) polar-orbiting satellites, the National Aeronautics and Space Administration (NASA) Aqua mission, and the European Organization for the Exploitation of Meteorological Satellites (EUMETSAT) Metop-A mission. Table 1 summarizes AMSU-A and AMSU-B channel specifications. AMSU-A, which has been designed for temperature sensing, has fifteen channels. Eleven among them are located within the oxygen absorption lines range (50–60 GHz). AMSU-B channels are located on the wings of the water vapor absorption line at 183.31 GHz, which makes it possible to retrieve humidity at a few levels of the atmosphere. In addition to sounding channels, AMSU-A and AMSU-B have so-called "window channels," which are mainly sensitive to surface and to low-atmosphere layers. AMSU-A and -B sample 30 and 90 Earth views with a nominal field of view of 3.3° and 1.1° respectively. The AMSU observation scan angle varies from −48° to +48°, which translates into ±58° incidence zenith angle variation. In regard to this, the angular dependence of measurements has to be taken into account for an optimal use of AMSU measurement in meteorological and climate applications. For each AMSU channel and for a given observation zenith angle, the brightness temperature has a maximal sensitivity at a particular height, but is sensitive to radiation emitted from adjacent layers with a decreasing weight. The relative contribution of each atmospheric layer to measured brightness temperature can be inferred from the so-called weighting functions (derivatives of transmittance with respect to altitude) usually associated with a peak at a well known altitude. For window channels the peak altitude is close to the surface. It should be noted that the peak altitude of the weighting function increases with an increasing zenith angle. When the instrument scans the Earth from nadir to ±58°, the optical path length between the satellite and the Earth increases. Figure 1 shows the weighting functions of a selection of AMSU channels at nadir and at 55° of zenith angle for a standard tropical atmosphere: AMSU-A channel 5 (53 GHz, noted as A5 hereafter); channel 6 (54.4 GHz, noted as A6 hereafter); channel 7 (54.9 GHz, noted as A7); AMSU-B channel 3 (183.31 ± 1 GHz, noted as B3); and AMSU-B channel 5 (183.31 ± 7 GHz, noted as B5 hereafter). A5 is weakly sensitive to the surface and gives the temperature in the low atmosphere (around 4–5 km). B5 peaks in the low atmosphere, between the surface and about 3 km whereas B3 peaks in the upper troposphere. Its weighing function has a maximal sensitivity height around 8–10 km in wet tropical conditions.

[8] In this study, channels B5, B3, and A5 are mainly used. B5 and A5 get information from the low troposphere and the atmospheric boundary layer. B3 observations are believed to be well informative about midtroposphere ex-
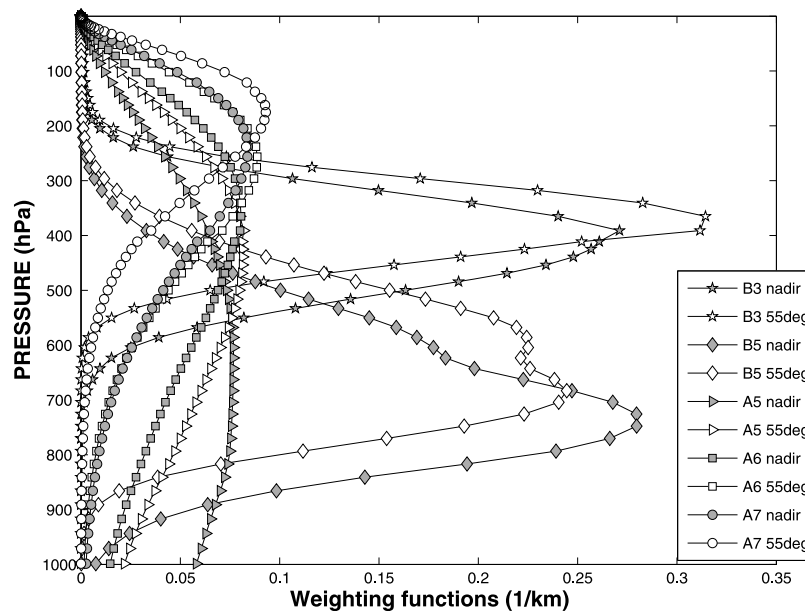
Figure 1. Weighting functions for a selection of AMSU channels and for a standard atmosphere.

changes with higher latitudes. *Roca et al.* [2005] showed the existence of extratropical dry air intrusion over the African monsoon region using Meteosat observations from the water vapor channel (5.3–7.1 μm), whose weighting function is comparable to B3 weighting function. A6 and A7 observations are used in some cases as their weighting functions peak in the same altitude range as B3.

[9] The area of interest is West Africa and the surrounding Atlantic Ocean, within the domain 30°W–45°E, 30°S–45°N, and subregions covered by the AMMA in situ measurements during 2005–2007, from the Gulf of Guinea to the Sahara desert.

2.2. AMSU Limb Adjustment

[10] As mentioned earlier, AMSU instruments observe the Earth with a large range of zenith angles. An effect of this is the variation of observed brightness temperatures (called Tb hereafter) along the scan line (limb effect) due to the longer path. For instance, the A6 Tb change from nadir to off-nadir positions reaches 14 K. Such a Tb change is quite stronger than the natural variations of the observed scene in a given atmospheric layer and must be corrected for an appropriate use of observations. This is particularly important for climate applications for which averaged Tb values in space and time are of prime importance. Techniques have been developed to adjust the observed radiance at a given angle to the radiance that would be measured at nadir. These techniques are based on either statistical or physical methods, and some of them combine the two approaches (*Wark* [1993] and *Goldberg et al.* [2001], among others). In this study, a statistical technique is used to adjust AMSU-A and -B observations to nadir. To do so, data from July 2006 over the globe (below 50° latitude north and south) were used to compute mean Tb differences between observations at a given scan position and observations at nadir (land and sea observations were separated to derive DIFF_SCAN). The

latter values are believed to be mostly related to view angle effect. For a given scan position, an observation is adjusted to nadir by correcting the observed Tb values. The limb-adjusted Tb values are equal to the observed Tb minus the Tb change from nadir to the considered scan position.

[11] Figure 2 shows the Tb variation along the scan line for A6 before and after limb adjustment. Results are for 1 year of data (2007). Plotted in Figure 2 are observed Tb averaged over January, February, and March (JFM) (Figure 2a); April, May, and June (AMJ) (Figure 2c); July, August, and September (JAS) (Figure 2e); and October, November, and December (OND) (Figure 2g). Figure 2 also plots limb-adjusted Tb averaged over JFM (Figure 2b), AMJ (Figure 2d), JAS (Figure 2f), and OND (Figure 2h). One should notice that the limb effect has been corrected for AMSU-A observations no matter what the season. This subjective evaluation of the limb adjustment procedure was completed with a case study on 18 August 2006 at 1800 UT. Figure 3 shows observed A5 Tb values along the orbits (Figure 3a), A5 limb-adjusted Tb values (Figure 3b), and a Meteosat Second Generation (MSG) infrared image from channel 10 (Figure 3c). It is difficult to highlight interesting atmospheric and surface features when looking at observed Tb values (Figure 3a). In particular, it is rather difficult to distinguish cloud signatures as seen in the MSG image, mainly because of the effect of observation angle. The limb-adjusted Tb values (Figure 3b) exhibit a smoother variation which lets one better analyze the scene: the temperature gradient associated with land/sea surface change is obvious, as well as the effect of clouds (over sea and over land) in agreement with MSG observations.

[12] A more rigorous evaluation of the limb adjustment procedure was performed using the radiative transfer model RTTOV [*Eyre*, 1991; *Saunders et al.*, 1999; *Matricardi et al.*, 2004]. The RTTOV model was fed by temperature and humidity profiles as well as surface temperatures taken from
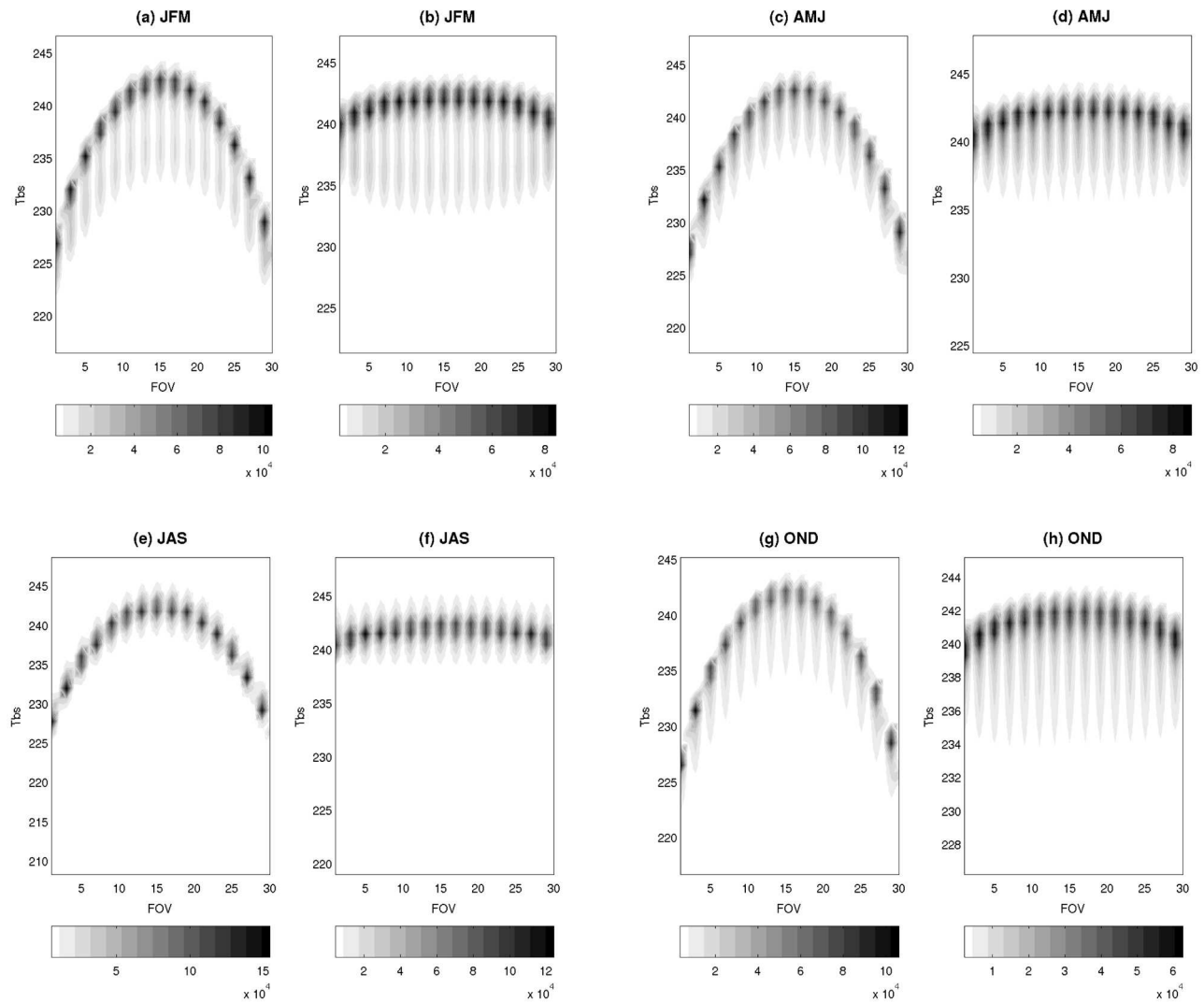
Figure 2. One year scatter plots of AMSU-A channel A6 as a function of the field of view (FOV). Shown are the (a) mean observed Tb values versus FOV averaged over January, February, and March (JFM) and (b) mean-adjusted Tb values versus FOV over JFM. (c, d) Same as Figures 2a and 2b but for April, May, and June (AMJ). (e, f) Same as Figures 2a and 2b but for July, August, and September (JAS). (g, h) Same as Figures 2a and 2b but for October, November, and December (OND).

analyses of the French 4D-Var global assimilation and meteorological forecast system Action de Recherche Petite Echelle Grande Echelle (ARPEGE). Simulations of AMSU radiances over sea/land at all AMSU zenith angles were performed and compared with observed Tb values. By the same token, AMSU radiances were simulated at nadir and compared with limb-adjusted Tb values. The limb adjustment procedure was evaluated using data collected over the area of interest (60°W–50°E, 30°S–45°N) and for two time periods: 1–15 June 2007 and 1–20 August 2007 (thus independent from the limb correction adjustment period). Global comparison statistics for A5, B5, and B3 are given in Table 2. Table 2 (column 3) gives mean biases and standard deviations of "observations minus simulations," which involve computations at all AMSU zenith angles. Column 4 in Table 2 gives similar statistics of "limb-adjusted observations minus simulations" in which the simulations were computed at nadir. And finally, correlations between

observations and simulations were computed before and after limb-adjusting observations. Note that no data cloud screening was performed. Table 2 shows that statistics for limb-adjusted Tb values are nearly as good as statistics for observed Tb values: there is a slight increase in standard deviation with limb-adjusted Tb values, and correlations are smaller for limb-adjusted Tb values but remain satisfactory. Figure 4 shows mean Tb values (observed and limb-adjusted) and mean Tb simulations (at all scan positions and at nadir) as a function of the AMSU-A scan positions for A5, A6, and A7 during August. For all channels, the simulation curves (at all incidence zenith angles and at nadir) are close to the observations and to the limb-adjusted observations. The smaller correlation obtained with limb-adjusted observations can be explained by the different asymmetries of the two Tb distributions. Thus, despite the difference in zenith angle, and in observed scenes, application of the limb correction procedure makes the interpretation and analysis of AMSU
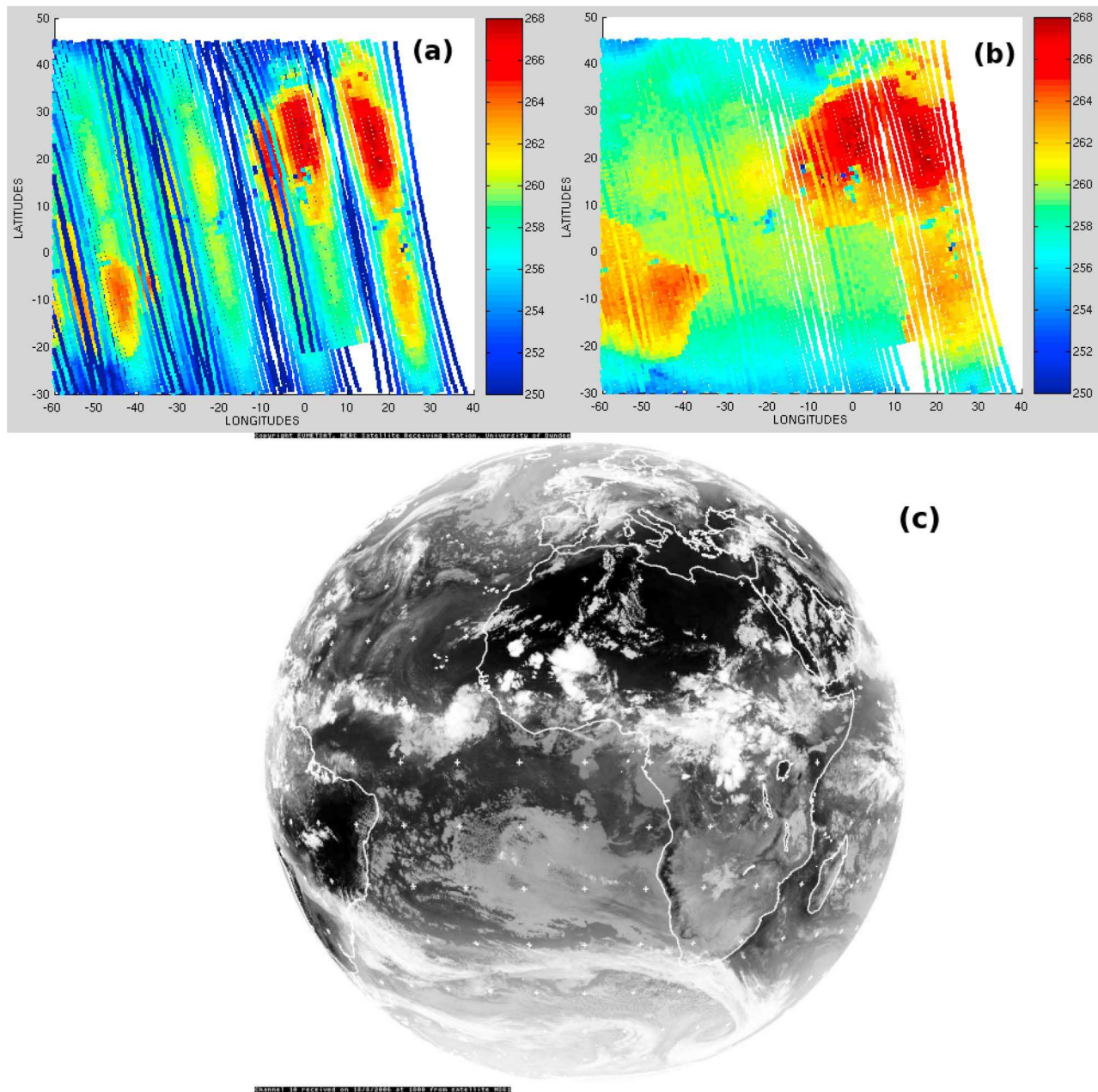
Figure 3. (a) AMSU-A channel 5 orbits as seen on 18 August 2006 at 1800 UT, (b) the corresponding limb-adjusted A5 observations, and (c) Meteosat Second Generation (MSG) infrared image as seen on 18 August 2006 at 1800 UT.

measurements rather easier than before. However, the "corrected observations" do not contain fully physically homogeneous data, but "nadir approximations."

2.3. Eight year AMSU Climatology

[13] Once limb adjusted, AMSU measurements were gridded through a time/latitude/longitude interpolation procedure. The grid resolution was chosen to be equal to 1 day/ 1 degree of longitude/1 degree of latitude. An interpolation method formerly developed by *Eymard et al.* [1989] to interpolate Sun-synchronous satellite data over global oceans was used. The method is based on the Cressman weighting function algorithm [*Cressman*, 1959]: data

weight decreases with the horizontal distance and time lag with respect to the Cressman radius. The radius is chosen as the distance at which data are independent. A one degree grid mesh was chosen for AMSU-A/B data to optimize the grid filling from data of variable footprint size with incidence and from successive orbits. The Cressman time radius is 3 days, and the chosen time interpolation step is 1 day, the grid time being 0700 UT each day. It oversamples the data flow from each satellite (exact repetition time, i.e., the same time over the same place, is 3 days). However, there are up to four satellites regularly spaced in time, so the chosen interpolation time allows one to benefit from the morning overpasses, which were given the highest weight to mini-

Table 2. Global Statistics of Observations Minus Simulations and of Limb-Adjusted Observations Minus Simulations

Channel	Period	Tb-SIM Mean/Standard Deviation (K)	TB_ADJ-SIM_NAD Mean/Standard Deviation (K)	Correlations (Tb and SIM)/ (Tb_adj and SIM_NAD)	Number of Observations
A5	1–16 June 2007	−0.071/1.075	0.16/1.141	0.979/0.942	822,038
	1–20 August 2007	−0.011/1.072	0.193/1.126	0.9770/0.9238	1,044,504
B5	1–16 June 2007	−2.228/6.220	−2.201/6.297	0.7417/0.7294	559,370
	1–20 August 2007	−2.074/6.079	−1.980/6.176	0.7365/0.7207	728,217
B3	1–16 June 2007	−0.421/3.990	−0.449/3.968	0.8871/0.8801	559,370
	1–20 August 2007	−0.356/3.943	−0.293/3.941	0.9013/0.8955	728,217

mize any surface or humidity diurnal cycle effects. For instance, *Chung et al.*, 2007, in agreement with previous studies, showed that the high-cloud diurnal cycle over tropical land regions has its maximum in the early evening.

[14] Orbital data were thus processed to produce a three-dimensional matrix over the study area over West Africa and the tropical Atlantic Ocean, with a resolution of 1° × 1° × 1 day. AMSU data from NOAA satellites 15, 16, and 17 were processed over the 2000–2007 period. Finally, yearly files were averaged to analyze the mean seasonal climatology of each AMSU channel. Comparisons with daily ECMWF Re-Analyses–Interim (hereafter noted as ERA-INT) available at 0.75° resolution and at 0600 were performed. Note that some AMSU channels are assimilated in the ECMWF model over ocean/land under several restrictions: one of these restrictions is that only channels receiving no or only a weak contribution from the surface are assimilated. In par-

ticular, B5 observations are not assimilated over land. Moreover, only clear air data are assimilated.

[15] Besides comparisons with ERA-INT, additional comparisons were performed with outgoing longwave radiation (OLR) interpolated data [*Liebmann and Smith*, 1996]. OLR estimations are derived from water vapor infrared channels on board operational meteorological satellites (NOAA Sun-synchronous series and geostationary satellites). In the present study, OLR data have been taken from the National Center for Atmospheric Research (NCAR) archive with a horizontal resolution of 2.5°.

2.4. On the Sensitivity of AMSU-A and -B Observations

[16] Figures 5a and 5b show the mean monthly maps for channels A5, A7, B5, and B3 for February (Figures 5a–5d) and August 2006 (Figures 5e–5h), using the swath angular
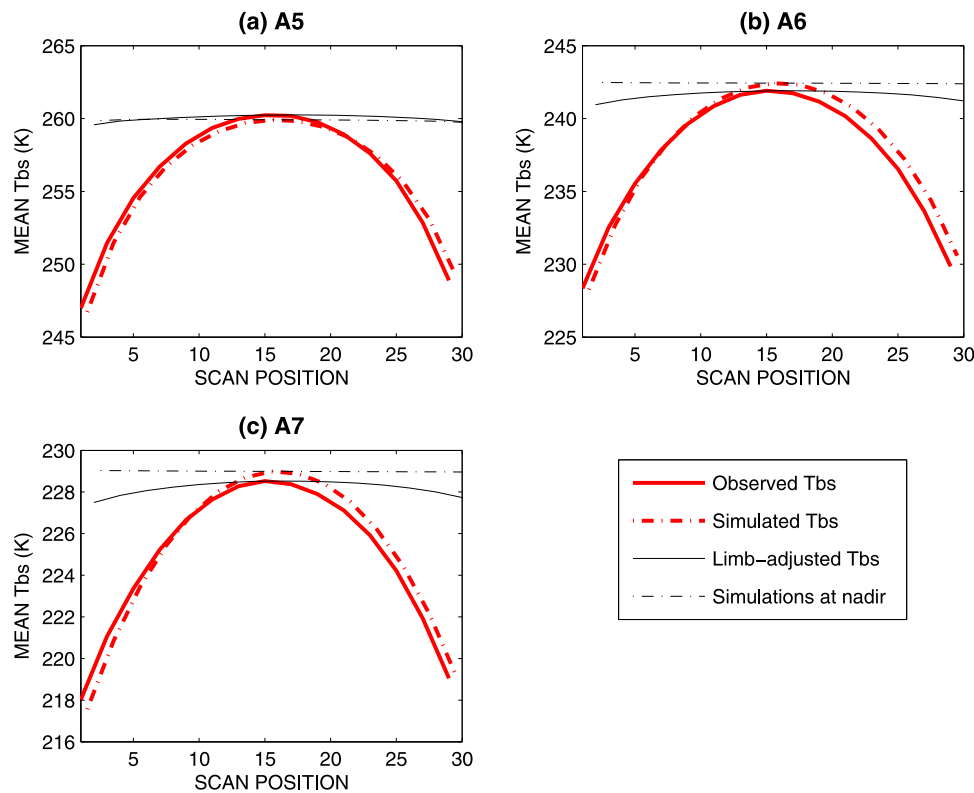
Figure 4. Mean Tb values (observed and limb-adjusted) and mean Tb simulations (at all scan positions and at nadir) as a function of the AMSU-A scan positions. Results are presented for (a) A5, (b) A6, and (c) A7 using data from August 2007.
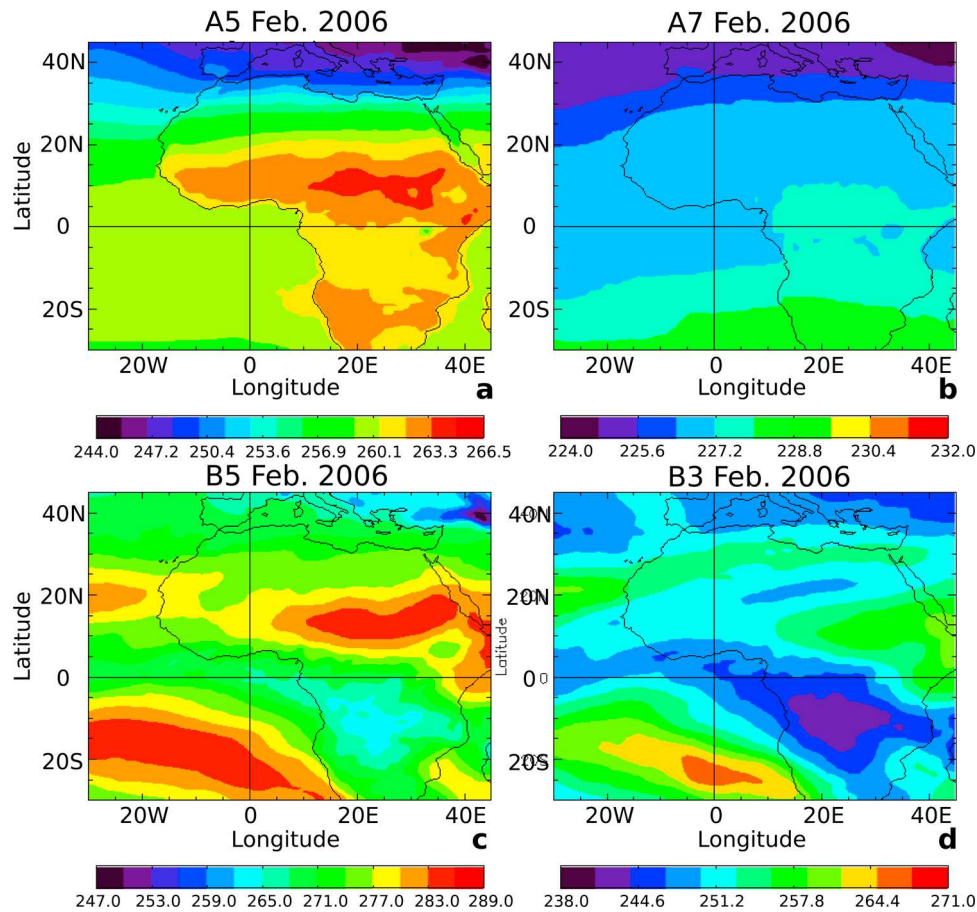
Figure 5. Mean monthly maps of AMSU brightness temperature channels for February 2006 for (a) A5, (b) A7, (c) B5, and (d) B3. Mean monthly maps of AMSU brightness temperature channels for August 2006 (e) A5, (f) A7, (g) B5, and (h) B3.

correction and the Cressman interpolation method presented in section 2.3. The four selected channels are weakly (A5 and B5) or even nonsignificantly (A7 and B3) sensitive to the surface because of the small total atmospheric transmission. The surface effect (emissivity and temperature) can be noticed on A5 Tb maps as sea observations are generally colder than land observations. This effect is still observed on corrected data thanks to the use of two different sets of limb adjustment coefficients to correct data over both sea and land. Although the B5 weighting function (Figure 1) indicates a significant sensitivity to the surface, the mean map of channel B5 for February (Figure 5a) does not show any detectable contrast between land and sea brightness temperatures, even in the driest climatic areas (coast of Western Sahara and Mauritania during the dry season). In clear air, the B3 and B5 brightness temperatures depend on the atmospheric humidity (through the absorption coefficient) and on temperature. *Soden and Bretherton* [1993], *Schmetz and Turpeinen* [1988], and *Roca et al.* [2005] established some correlations between the Meteosat/Spinning Enhanced Visible and Infrared Imager (SEVIRI) water vapor infrared channel observations and relative humidity fields around 400 hPa. In microwave and infrared frequency ranges, the radiative transfer physics is rather similar in clear air. *Buehler and John*

[2005] and *Jimenez et al.* [2005] thus retrieved the upper tropospheric humidity from B3 Tb in clear air. Can we therefore expect that both B3 and B5 be used to describe the humidity variability in our region of interest?

[17] To answer this question, comparisons with ERA-INT fields were performed. ERA-INT relative humidity fields at pressure levels ranging from 200 to 500 hPa and from 700 to 975 hPa were respectively correlated with B3 and B5 using data from 2006. In agreement with their weighting functions, B3 and B5 were found to fit best with humidity fields at 350 hPa and 750– 775 hPa for B3 and B5, respectively. Figure 6 shows the mean relative humidity field (RH) from ERA-INT for February and August 2006 at these two levels (noted as RH350 and RH775 hereafter). The main patterns between Tb and humidity fields are similar: dry (moist) areas correspond to high (low) Tb. In both cases, the Intertropical Convergence Zone (ITCZ) signature is obvious (high humidity/low Tb) and is flanked by dry zonal bands corresponding to the descending branches of the Hadley cells (low humidity/high Tb). A further comparison of the standard deviation and of the three first orthogonal modes (empirical orthogonal function (EOF) analysis) over the years 2005, 2006, and 2007 for both AMSU B3/B5 and ERA-INT relative humidity at levels equivalent to those of
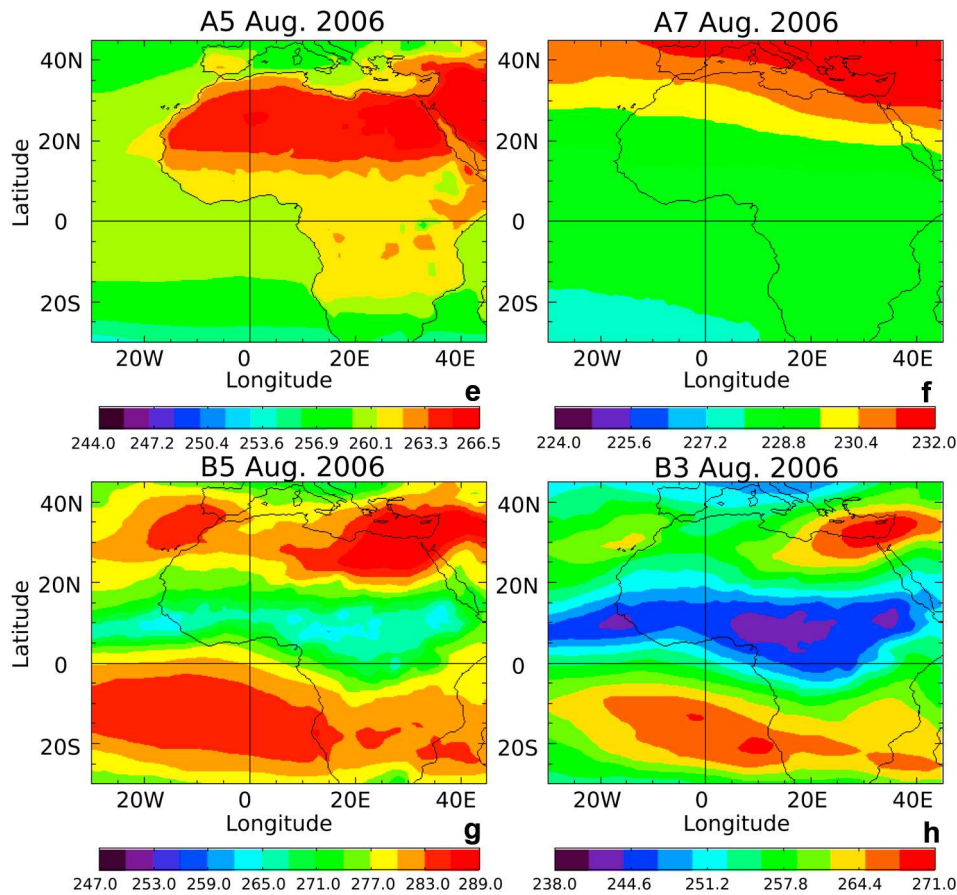
Figure 5. (continued)

the correlation analysis led to the same level selection. This comparison is shown in Figure 7a for B3 and Figure 7b for ERA-INT RH350. Higher-variation areas, though with a different extension, are in matching locations (over eastern Mediterranean Sea and southern subtropical Africa) as shown by standard deviation maps. Some of the differences are consistent with the different locations of maxima in mean maps. For the three modes, maxima and minima are inverted between both fields. This is due to the sign of variation being different (for maximal humidity, Tb is minimal); the first mode corresponds to the seasonal latitudinal variation over the African continent, with maxima during the boreal summer and winter (accounting for 36% of the total variance of B3 Tb (18% for RH350)). The second mode shows the half-season variations (maxima in April and October) over the equatorial Africa and Sahel (7% variance for B3). The third mode depicts intraseasonal variability over the domain, with dominant areas over the Sahara desert and the monsoon areas in Africa and the Gulf of Guinea (5.6% variance). The second and third modes are inverted in RH350 EOF, with respect to B3, and the agreement between features from the two data sets is rather poor. A lack of assimilated B3 data in the model at intraseasonal scale due to clouds could be an explanation. A more detailed comparison of intraseasonal variations is presented in section 3.2. Both the correlation field and the agreement between EOF patterns are better for B3 than for B5 (average correlations 0.75 and 0.5, respectively). This can be due to the fact that B3 data are assimilated in the model (in clear air over sea/land), which is not the case for B5 (only over sea). The lack of assimilated data (satellite and in situ) may lead to large errors in the low atmosphere, because of small-scale surface-atmosphere interaction processes over land and ocean.

[18] AMSU B3 and B5 observations can thus be used as "proxies" to analyze the main humidity variations. In the following, ERA-INT relative humidity fields are used for comparison purposes. Specific humidity fields produced similar comparison results (not shown). The atmospheric temperature in the layer should theoretically influence the Tb. However, when statistical tools are applied to A5 and B5, either A6 or A7, and B3 (correlations between variability modes and fields), they fail to establish a significant contribution of the temperature in B3–B5 Tb and perforce to show this sensitivity.

[19] Besides a sensitivity to the atmospheric humidity, the selected microwave observations are also sensitive to rain/clouds. At low microwave frequencies (1 to 60 GHz), the effect of clouds and rain (light to medium) is well described by the Rayleigh scattering, which causes an increase in Tb.
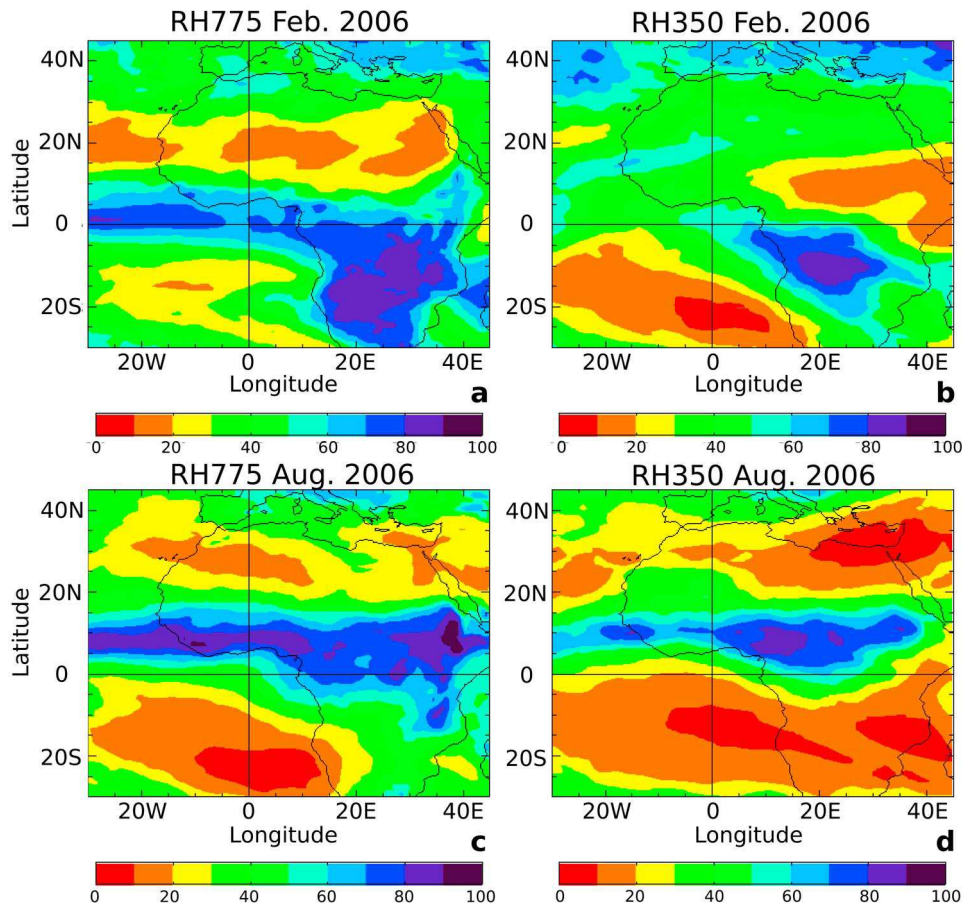
Figure 6. Mean relative humidity for (a and b) February and (c and d) August 2006 from ERA-INT reanalyses. Note that the color scale is from red to blue, to make it easier to see the comparison with B5 and B3 mean fields.

As the relative size of droplets and ice crystals increases with respect to the electromagnetic frequency, the Mie scattering progressively dominates. This induces strong depression of the brightness temperature. Rain retrieval using imaging radiometers such as the Special Sensor Microwave Imager (SSMI) and the Tropical rainfall Measuring Mission (TRMM) Microwave Imager (TMI) are based on these physical properties, at frequency ranges 10–90 GHz [e.g., *Spencer et al.*, 1989; *Mohr and Zipser*, 1996]. In the temperature sounding range (50–60 GHz), only the very high rain (center of large convective clouds, a few kilometers in diameter) may impact the signal, but it is strongly attenuated by the spatial averaging within the footprint (48 km at nadir), then by the interpolation procedure into the 1° grid. In contrast to this, for B3/B5 humidity observations, the Mie scattering dominates, even for light rain events [*Ulaby et al.*, 1981]. *Greewald and Christopher* [2002] estimated that the Tb depression by cold clouds (Tb < 240 K) in the 183 GHz band with respect to clear air is small for nonprecipitating clouds (around 1.4 K), but can reach up to 15 K for deep convective clouds. This property was used by *Hong et al.* [2008] to establish a climatology of tropical convective clouds with AMSU-B. When examining AMSU-B B5 and B3 images in Figures 5c and 5d and

Figures 5g and 5h, the center of deep convection areas can be seen and are associated with the lowest Tb values. Despite the averaging effect in the footprint (16 km at nadir) and the further averaging into 1 square degree meshes, large and intense convective systems are clearly depicted in space and in time as illustrated in the longitude-time Hovmoeller diagram for B5 during the 2006 monsoon season over the latitudes 7°–12° (see Figure 8a). The Tb difference between clear air and convective clouds reaches several degrees between minima (255–257 K, dark blue color) and surrounding air (260–265 K, medium blue). As previously observed by *Hong et al.* [2008], B5 offers a better contrast between clear air and convective clouds than B3 because of the higher brightness temperature in clear air. The B5 Hovmoeller diagram shows that the monsoon development is characterized by two important convection initiation zones at 35°E and 15°W (near the western coast). The western propagation of big convective systems becomes obvious between June and September.

[20] The OLR is often used to monitor the convective activity, since the colder the brightness temperatures in the thermal infrared, the deeper the clouds. The OLR Hovmoeller diagram (Figure 8b) is for the same area and the same period. AMSU and OLR data have different spatial
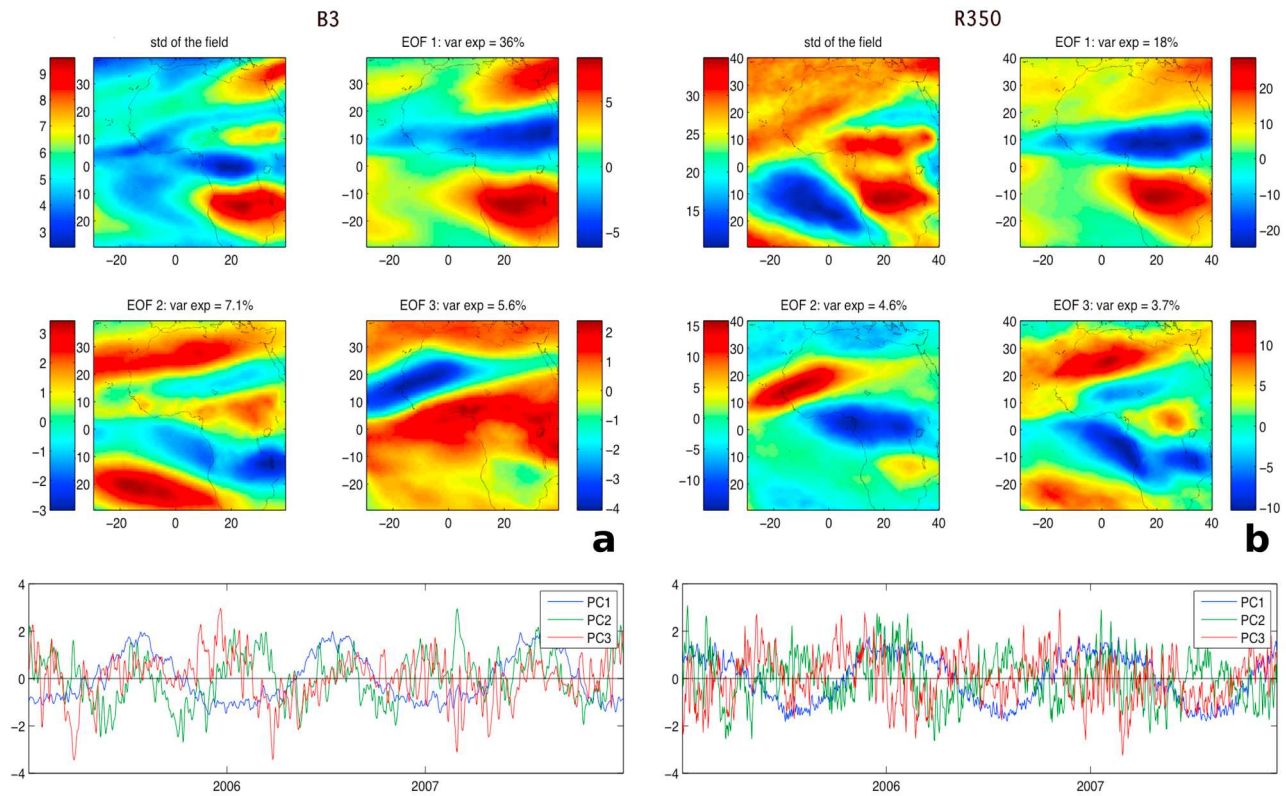
Figure 7. (a) Standard deviation (top) and first three empirical orthogonal function (EOF) modes of B3 Tb values, and (b) ERA-INT relative humidity (top) at 350 hPa over years 2005–2007. The corresponding time series are given in Figures 7a (bottom) and 7b (bottom). Note that the second and third mode of RH350 are inverted, compared to the B3 ones.

and time resolutions (3 days, 1° for AMSU; 1 day, 2.5° for OLR), which induce differences between the two diagrams. Even though the two data sets are different and differently processed, the two convection development areas (east and west of the continent) are clearly seen on OLR, as well as the large convective area between July and September at 10°E–20°E. Moreover, large systems propagating to the West (see for example the one at 20°W–30°W for August, and the one propagating from 10°E to 20°E for September) are clearly depicted on both diagrams. The dry areas of April–May, in yellow-red, can be seen on both diagrams.

3. Analysis of AMSU Data Seasonal Variations

3.1. Mean Features

[21] In this section, a mean AMSU climatology is used. It was obtained by averaging all annual data sets (8 years). A similar averaging procedure was applied to ERA-INT analyses. Figure 9 and Figure 10 present the main features of AMSU A5 (Figure 9a) and B5 (Figure 9b), ERA-INT geopotential difference between 700 and 925 hPa (Figure 10a), and relative humidity at 775 hPa (Figure 10b). Mean maps are plotted over a large domain covering the monsoon area over the continent (30°W–40°E, 30°S–40°N) from April to September. Latitude-time Hovmoeller diagrams are plotted in Figure 11 for the longitude band 10°W–5°E for A5, A7, B5, and B3. Figure 12 shows the latitude-time diagram for ERA-INT data. In the following, main comparison features

are discussed to evaluate the relevance of AMSU Tb values for analyzing the monsoon area.

3.1.1. Humidity Features

[22] Mean maps of relative humidity from April to September at 775 hPa are compared with B5 maps. In both maps, the dominant features are (1) the ITCZ (high ERA-INT humidity, low AMSU Tb due to humidity and clouds) located between 10°S and 15°N, depending on the longitude and the month; and (2) the dry areas apart from the ITCZ in the North and South Hemispheres, in the downward branches of the two Hadley cells. However, if the agreement between ERA-INT and B5 is maximal in April, then the evolution of the monsoon band and dry areas is slightly different:

[23] 1. ITCZ patterns: as illustrated in Figures 10 and 11, the convection band is more zonal in RH775 than in B5 (June, in particular), and the latitude/time diagram shows that the monsoon band center remains at latitude lower than 10°N in ERA-INT RH775, whereas it reaches 11°N–12°N in B5. Inside the convective band, three humidity/convection maxima can be identified in B5 maps (Figure 10b) along the western coast (15°W) at 10°E–20°E and at 35°E. There is a good agreement between RH775 and AMSU B5 data for the first one, but the second one remains close to the coast in RH775 data (10°E), while the third one is close to 40°E and at latitudes 5°–12°N. Another difference is that there is no monsoon "jump" in the end of June in ERA-INT fields, contrary to B5 and B3 (Figures 11c, 11d, 12c, and 12d), which show a 4° latitude change in the monsoon
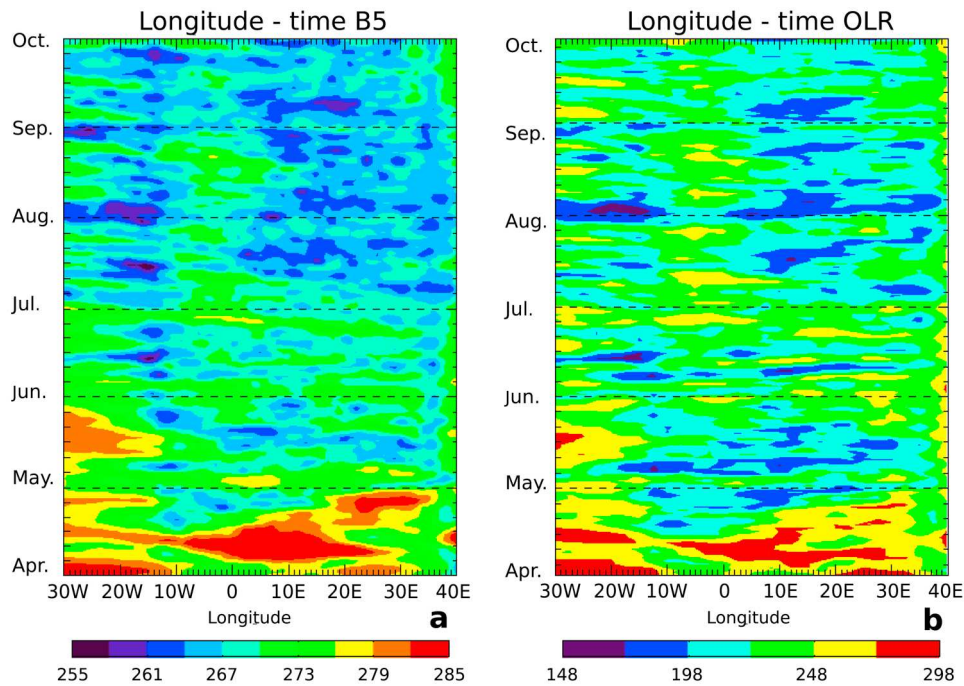
Figure 8. Longitude-time diagrams of (a) B5 Tb and (b) OLR for April–September 2006. A 3 day smoothing was applied to OLR data for a better comparison.

center between June and July. *Sultan and Janicot* [2003] showed evidence of the monsoon jump using OLR data. As the B5/B3 minima are due to deep convection imbedded in a wide humidity band, it is very likely that the monsoon jump can be detected using B5, as well as with OLR. Note that the high humidity envelope is more continuous, as is the ERA-INT humidity field, but it reaches higher latitudes. However, the humidity time patterns at 350 hPa (Figure 12d) by the end of April, 1 June, second half of July and 1 September are correlated with the lowest B3 Tb (Figure 11d).

[24] 2. Dry areas apart from the ITCZ: dates of maximal dryness in the Northern Hemisphere as seen by RH775 fields agree with those of B5 (beginning of May, mid-June, end of July, mid-September), as seen in Figures 9 and 10. At 350 hPa, the general evolution is consistent with B3, but with a scattered pattern. Another discrepancy is that the RH775 band, as noticed on monthly mean maps (Figure 10), is more zonal, has a much weaker maximum in eastern Africa compared to B5, with also an opposite evolution (highest values in July for B5/B3 and lowest values for RH775). In western Africa (0°–15°W), the dry area does not weaken after June, contrary to B5. Finally, the northern dry band has an East–West contrast in B5 with very dry values east of the Greenwich Meridian.

[25] The Southern Hemisphere dry band has a smaller extent in RH fields, and its maximal intensity is in July–August, instead of June for B5. This band is wider at 350 hPa than at 775 hPa (Figures 12d and 12c), contrary to B3/B5 (Figures 11d and 11c). Both dry bands are shifted to the south, with respect to AMSU data (20°N–25°N and 15°S–20°S for RH data compared to AMSU ones: 27°N–30°N and 10°S–15°S). Moreover, they do not show the correct time evolution (large phase error).

3.1.2. Temperature Features

[26] The prominent feature is the seasonal development of a large warm area in the lower atmosphere over the Sahara (see A5 maps in Figure 9a). This pattern, also noticed when looking at latitude-time diagrams over longitudes 5°W–10°E (Figure 11a and 11b), does not extend to higher altitude, as seen in the A7 diagram. However, the A7 seasonal warming at high latitude is well correlated with the warm area development seen in A5. This seasonal heating of the low atmosphere over the Sahara, with a maximum in July centered at 25°N, 5°W corresponds well to the so-called heat low (HL), as described by *Lavaysse et al.* [2009] and *Chauvin et al.* [2010]. The heat low is thought to be one of the major atmospheric structures which govern the overall monsoon seasonal evolution. It is strongly correlated with the northward displacement of the monsoon rain band, as discussed by *Sultan and Janicot* [2003], *Sultan et al.* [2003], and *Ramel et al.* [2006] among others. *Drobinski et al.* [2005] showed the importance of Hoggar Mountain in the summer location of the heat low using National Centers for Environmental Prediction (NCEP) reanalyses. In the following, the A5 patterns are compared with some of the meteorological fields usually used for the heat low analysis [*Lavaysse et al.*, 2009; *Chauvin et al.*, 2010]: surface pressure and geopotential difference (700–925 hPa, hereafter noted ∂Geopt). These fields are used to depict the heat low features and evolution. Figure 12a and 12b show the latitude-time diagram for the surface pressure (mean sea level (msl)) and ∂Geopt, respectively. Compared to A5 features, the most similar field (extension, seasonal evolution) is found to be the geopotential difference (∂Geopt). As ∂Geopt is a measure of the heat content between heights 925 and 700 hPa, it is proportional to the mean temperature in this layer, whereas A5 Tb are directly related to the weighted
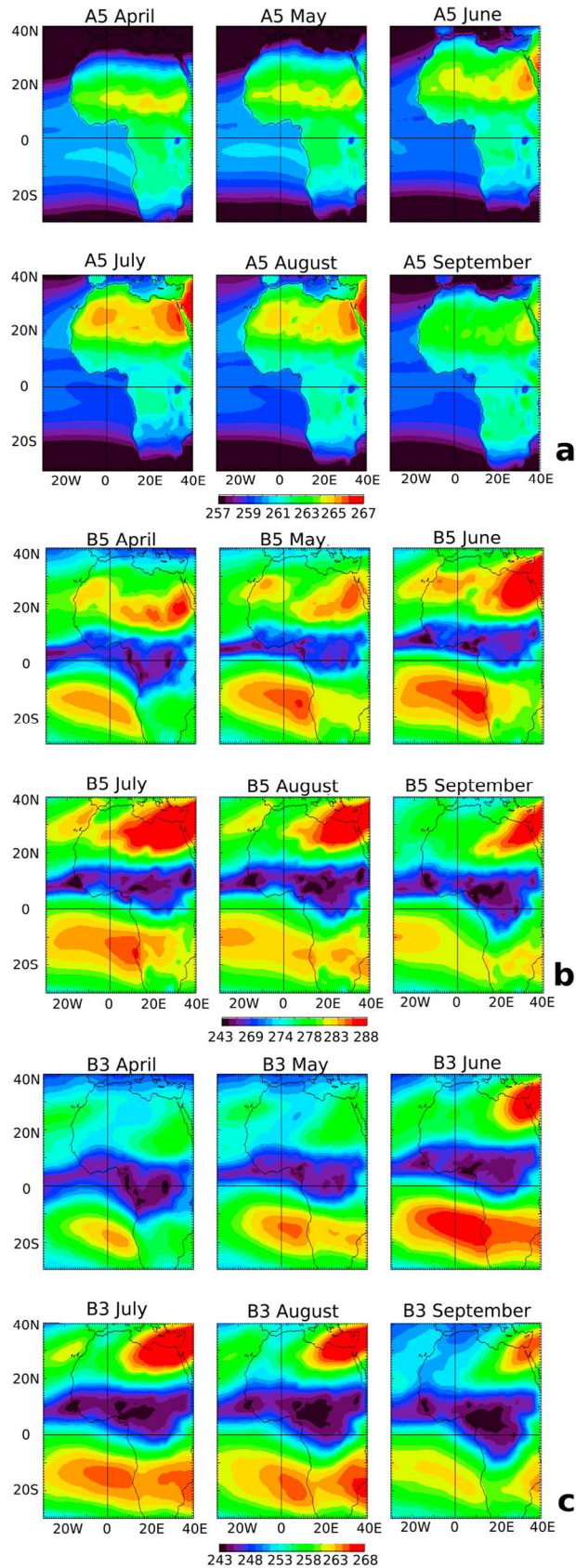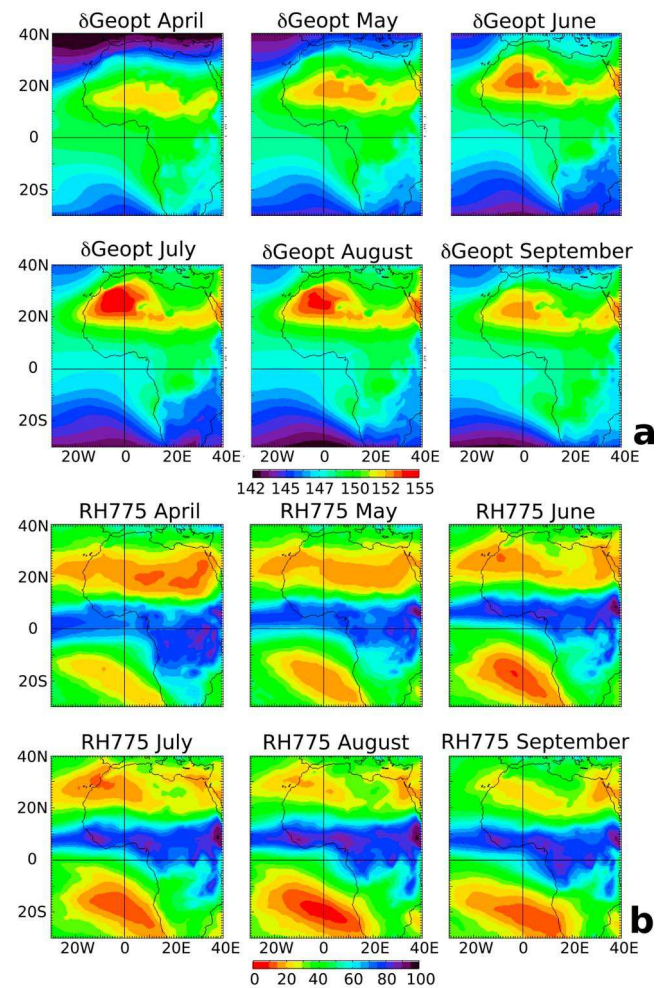
Figure 9. AMSU climatology (2000–2007) monthly mean maps from April to September for (a) A5, (b) B5, and (c) B3.

integrated atmospheric temperature in a wide layer ranging from the surface to about 600 hPa.

[27] The A5 channel can hence be used to monitor the HL. A more in-depth comparison with ∂Geopt reveals that the HL development is more continuous from April to July in the ∂Geopt fields, and it starts around the Hoggar Mountains, then enlarges upon a wider area. Moreover, A5 mean monthly maps show a zonal band, with maxima around 20°E and 35°E in May–June, and the HL area is not warmer than the Red Sea area. This is not observed in ERA-INT fields (Figure 10). Another feature on A5 maps is the cooling over the ocean south of the equator, maximal in July, contrasting with a warming continental region at 10°S–20°S. This warm area is clearly depicted in the ∂Geopt in September, but the atmosphere cooling over the ocean seems very weak.

3.1.3. Main Conclusions

[28] In summary, the AMSU channels clearly depict the main features of the West African monsoon: a meridian shift of the ITCZ with the monsoon onset at the end of June and a development of the Saharan heat low in the low troposphere, associated with a phased upper atmosphere warming at 30°N–

Figure 10. ECMWF climatology (2000–2007) monthly mean maps from April to September for the (a) geopotential difference (700–925 hPa) and (b) relative humidity at 775 hPa over the 8 years 2000–2007.
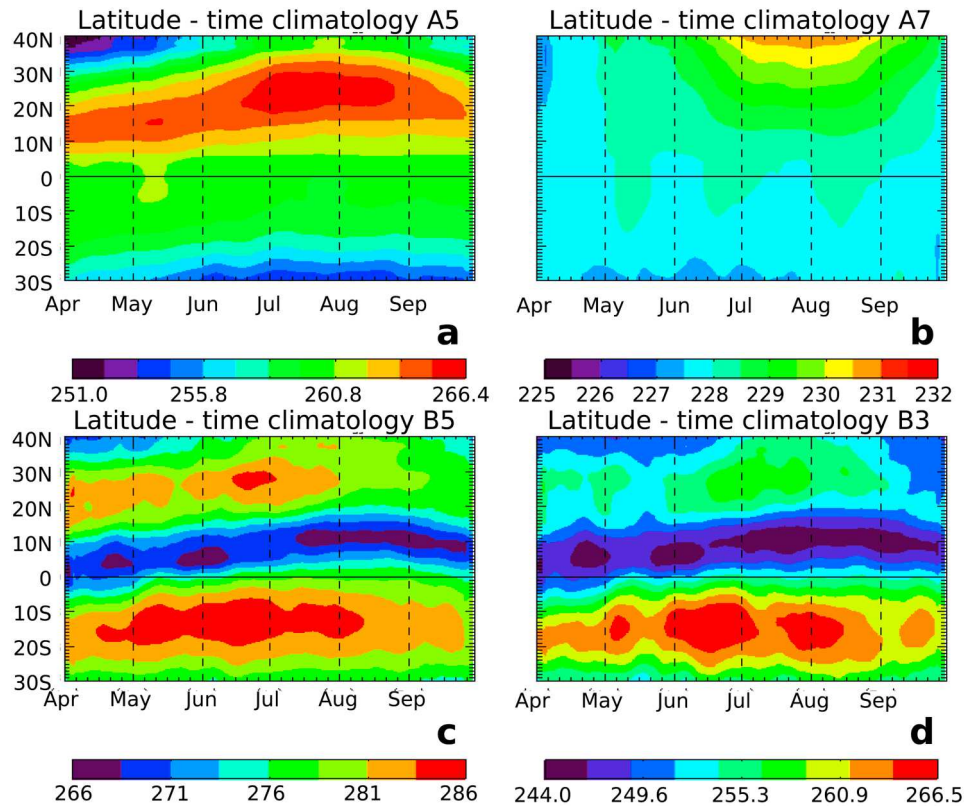
Figure 11. AMSU Tb climatology latitude-time diagrams for the monsoon season (April–September) for (a) A5, (b) A7, (c) B5, and (d) B3.

40°N. AMSU-B data show in addition dry patterns on both sides of the ITCZ, which have not been yet analyzed, with a particularly hot and dry area in eastern Africa and Arabia.

[29] Comparison between AMSU-B channels and ERA-INT humidity climatologies indicate that the ERA-INT mean ITCZ zonal patterns are not constrained enough by the dry areas as it is suggested in AMSU data. In addition, there is no jump in July above 10°N after a clear monsoon onset, as previously shown by *Agusti-Panareda et al.* [2009a, 2009b]. Another discrepancy is the distribution of dry air, principally in the Southern Hemisphere, where ERA-INT dry area has a smaller extension and intensity, particularly at low altitude, and is shifted to the south. This excess troposphere humidification by the ocean could possibly be due to a too weak atmospheric boundary layer stratification in the model, letting humidity spread into the troposphere. This was first discussed for ECMWF in subtropical zones (ocean upwelling areas) by *Esbensen et al.* [1993].

[30] Despite a good agreement for the HL location in summer, some differences between A5 and ERA-INT geopotential difference are noticed, both in the Saharan band (eastern wide warm area), and south of the equator over the ocean. They can probably be related to differences between AMSU humidity channels and ERA-INT relative humidity, in eastern Africa (too wet) and south of the equator (too wet at low level).

[31] The AMSU data seem to be well suited to show the atmospheric temperature and humidity features in the monsoon area. This is of high interest since a large amount of available AMSU observations are still rejected from the

assimilation systems (effect of land surface and of clouds). For instance, over land surfaces observations from AMSU-B channels 1, 2, and 5 are still entirely rejected from the models. AMSU data are thus a useful complementary tool, with OLR data, to analyze the monsoon characteristics.

3.2. A Focus on 2005–2007 African Monsoon Seasons

[32] The 8 year data set makes it possible to examine the intraseasonal variability and the potential physical links between different regions. In this section, a preliminary analysis of years 2005 to 2007 is presented. During the AMMA program, the 3 years 2005, 2006, and 2007 were investigated through intensified networks of radiosoundings and surface stations, including GPS, through the so-called Extended Observing Period. AMSU data from the 3 years are analyzed in this section. Some of the AMMA data were assimilated in the ECMWF model, and helped improve the analysis, particularly in 2006 [*Agusti-Panareda et al.* 2009a, 2009b].

3.2.1. Hovmoeller Diagrams

[33] Figure 13 shows the latitude-time diagrams in the longitude band 10°W–5°E for channels A5 (Figure 13a), B5 (Figure 13b), and B3 (Figure 13c). The same diagrams are shown in Figure 14 for ERA-INT ∂Geopt (Figure 14a), RH775 (Figure 14c), and OLR (Figure 14e). The mean correlation over the 3 years for the same longitude band are plotted in Figure 14: A5-∂Geopt (Figure 14b), B5-RH775 (Figure 14d), and B5-OLR and RH775-OLR (Figure 14f). The three successive monsoon seasons can thus be compared:
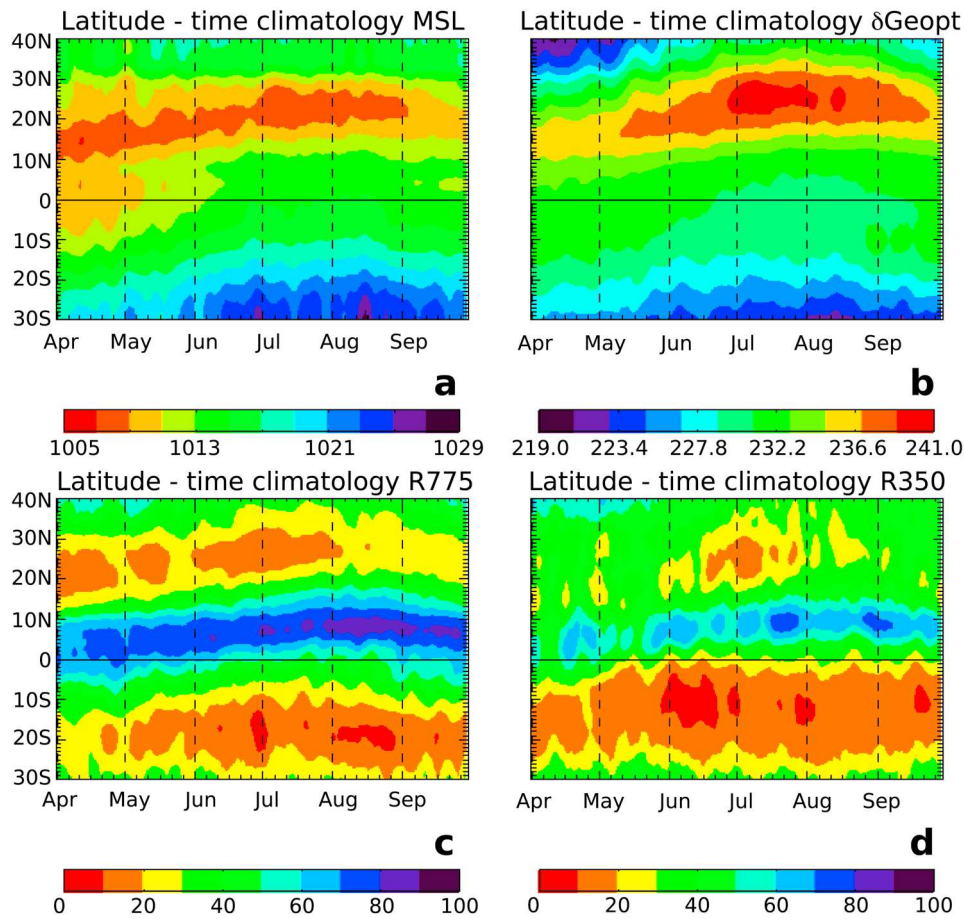
Figure 12. ERA-INT climatology. Latitude-time diagrams for the monsoon season. (a) Mean sea level (msl) pressure, (b) geopotential difference (700–925 hPa), (c) relative humidity at 775 hPa, and (d) relative humidity at 350 hPa. As in Figure 10, color scales are from red to blue in relative humidity panels.

[34] 1. Atmosphere heat content: From the A5 diagram, the HL seasonal development is different from one year to another: in 2005, an early warming occurs with a first maximum in April. Its development is continuous to the north, then the HL takes place at the end of June (reaching its northern maximal location) and stays until the end of August, with one more warm period in September; in 2006, warming during boreal spring is more scattered, and the HL gets established in the beginning of July, with a maximal extension to north in August; the spring warming starts later in 2007 (end of March) with a continuous development as in 2005, but the first maximum is observed in May. Despite an early installation of the HL (mid-June), the northern extension occurs in August, followed by a rapid decay as in 2006. Comparison of A5 diagrams with ∂Geopt shows that the best agreement occurs in 2007. In 2005, the spring evolution is different (large warming in May–June), and the only clear agreement in 2006 is for the scattered spring development. The correlation coefficient is nevertheless good (0.9) for the HL. It is much lower in the Gulf of Guinea (10°S–20°S) where low-atmosphere heat content does not vary similarly in both data sets. The weak amplitude of variations prevents from easily interpreting this low correlation.

[35] 2. Humidity at low and high altitude (B5 and B3 diagrams in Figures 13b and 13c) highlights the monsoon band seasonal and intraseasonal evolution. The main difference between the two channels consists of occurrences of humidity exchanges with northern latitudes in the high atmosphere (B3) more often than closer to the surface (B5). B5 and A5 variations are well correlated at highest latitudes north and south (Figure 15a), where mid-latitude winter lows and highs induce synchronized variations of temperature and humidity over sea. Although the general latitudinal variation of the correlation coefficient is similar for ∂Geopt and RH775, its low value is probably due to model weakness in representing the humidity for this region: the A5-∂Geopt correlation is good, contrary to the one between B5 and RH775, particularly in the Gulf of Guinea. Note that the correlation between B5 and RH775 is significant only in the ITCZ, which is dominated by the strong seasonal variation. The good qualitative agreement between B5 and OLR diagrams (Figures 13b, 13c, and 14e) is confirmed by the high correlation coefficient at all latitudes except in the Gulf of Guinea near 10°S, where the atmosphere is mostly clear (Figure 14f).

[36] When comparing the three monsoon seasons, the monsoon onset occurs at different dates, as seen on B5 and
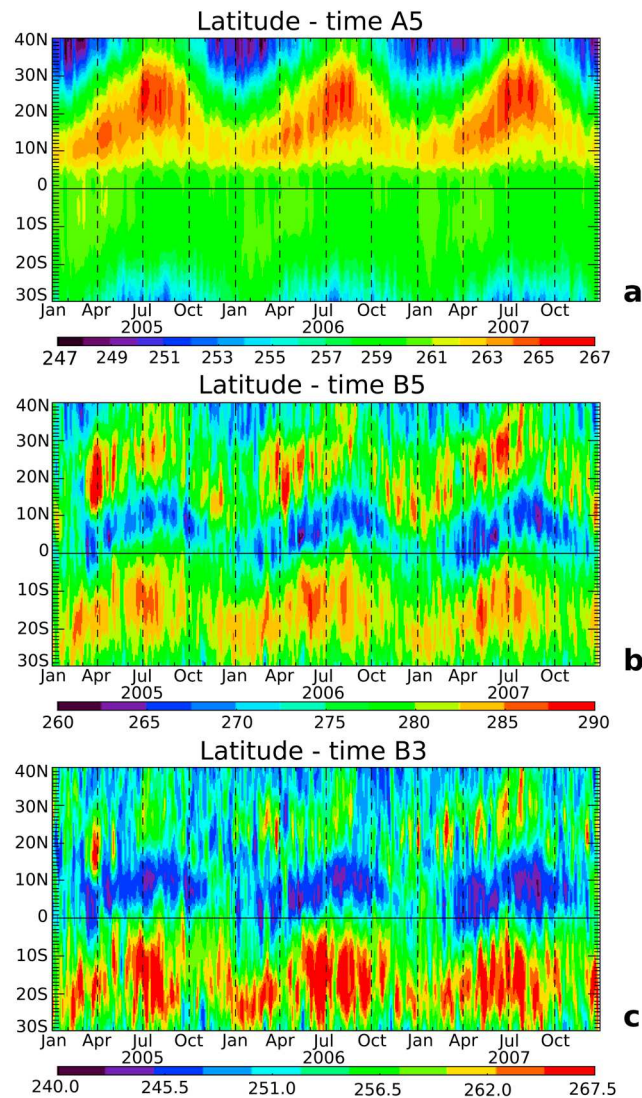
Figure 13. Latitude-time diagrams for years 2005 to 2007, longitude band 10°W–5°E for (a) A5, (b) B5, and (c) B3.

B3 Hovmoeller diagrams, as well as on OLR (Figure 14e): it occurs early in 2005 (around 20 June) and late in 2006 (around 10–13 July). In 2007, B5/B3 and OLR seem to disagree: humidity is high since mid-June, but convection at 10°N starts rather late (around 10 July as in 2006). End of June is the time of the transition phase of the onset where the convective activity state is rather fuzzy. It is characterized in B5/B3 by a high humidity content and in OLR by a weak convective activity, but both data show an activation of convection after 10 July. They better agree when considering only the AMSU Tb minima, corresponding to deep convection. During the 2007 season, the humidity band is wider in latitude than during the two previous seasons (see the B3 diagram). This season is associated with a wetter atmosphere over the Gulf of Guinea from July to September. Despite the fact that the monsoon band is located too far south (see the previous section), the wider humidity band is

also depicted in RH775 diagram (Figure 14c) but later (in August and September).

[37] From AMSU channels diagrams, the HL and monsoon onsets and intraseasonal variations can thus be monitored. The development of the monsoon appears as a succession of events (wet/dry), which seem to be connected with variations in the two dry areas apart from it in latitude: see for example the dry intrusions from the north by end of March 2005, beginning of April 2006; the connections in humidity at high altitude across the Sahara, up to the Mediterranean Sea (B3); the links between wetter periods in the Gulf of Guinea; and the wider humidity band in the convective band. Dry intrusions from the Mediterranean Sea were investigated by *Roca et al.* [2005] using Meteosat water vapor data. These connections can be related to the African Easterly Jet modulations affecting the whole area, and/or to the modulations of the two anticyclonic areas, Azores and St. Helen highs [*Janicot et al.*, 2008].

3.2.2. Wavelet Analysis

[38] To further investigate the intraseasonal variability, a wavelet analysis was performed over time series taken along the Greenwich Meridian (5°W–5°E) at the three latitudes (HL: 20°N–30°N; monsoon: 5°N–15°N; Gulf of Guinea (GG): 20°S–10°S). A high pass filter was applied to remove the seasonal variation mode, with a scale cutoff at about 90 days. The wavelet spectral analysis (Figure 16) reveals the dominant variability mode periods and their occurrence within the time series. By integrating the spectral energy over the time, the major modes can be characterized. In order to identify modes associated with the monsoon development, a second integration over monsoon season (April–September) was made (plotted with a dashed line). Finally, the robustness of modes was checked by processing the 8 year time series. They are compared with ERA-INT wavelet diagrams, and with OLR in the ITCZ.

[39] In the following, first results are given for each latitude band:

[40] 1. Heat low (20°N–30°N): for A5 (Figures 16a and 16b) and B5, the dominant mode is observed for a 35–40 day period. It is as well observed on the 8 year data set, over the year and over the monsoon season. As seen in Figure 15a, it occurs nearly continuously over the 3 years. A shorter mode, for a period 8–10 days, is also found in A5 wavelet time series, with a slightly higher occurrence during the monsoon season (maximal between April and September 2005, then from winter to summer 2006, but less continuously, and more or less disappearing in 2007). Contrary to the 40 day mode, this one is observed in ERA-INT ∂Geopt (Figure 17a) only during the monsoon season (with a weaker amplitude). Another intraseasonal mode, with a main period of 18–20 days, can be observed on A5 and B5, but with a larger spectral variability. This mode is found in ERA-INT ∂Geopt and RH, with no seasonal variation of occurrence. Note that the wavelet signal for periods over 90 days is outside of the significance domain because of edge-effects.

[41] 2. Monsoon band (5°N–15°N): the B5 wavelet diagram (Figures 16c and 16d) is dominated by two modes, at 22 and 40 days (also found in the 8 year wavelets). They are also obvious in the OLR wavelet time series (Figure 17c), whereas the first one strongly dominates in ERA-INT RH wavelet plot (Figure 17b). The 40 day mode
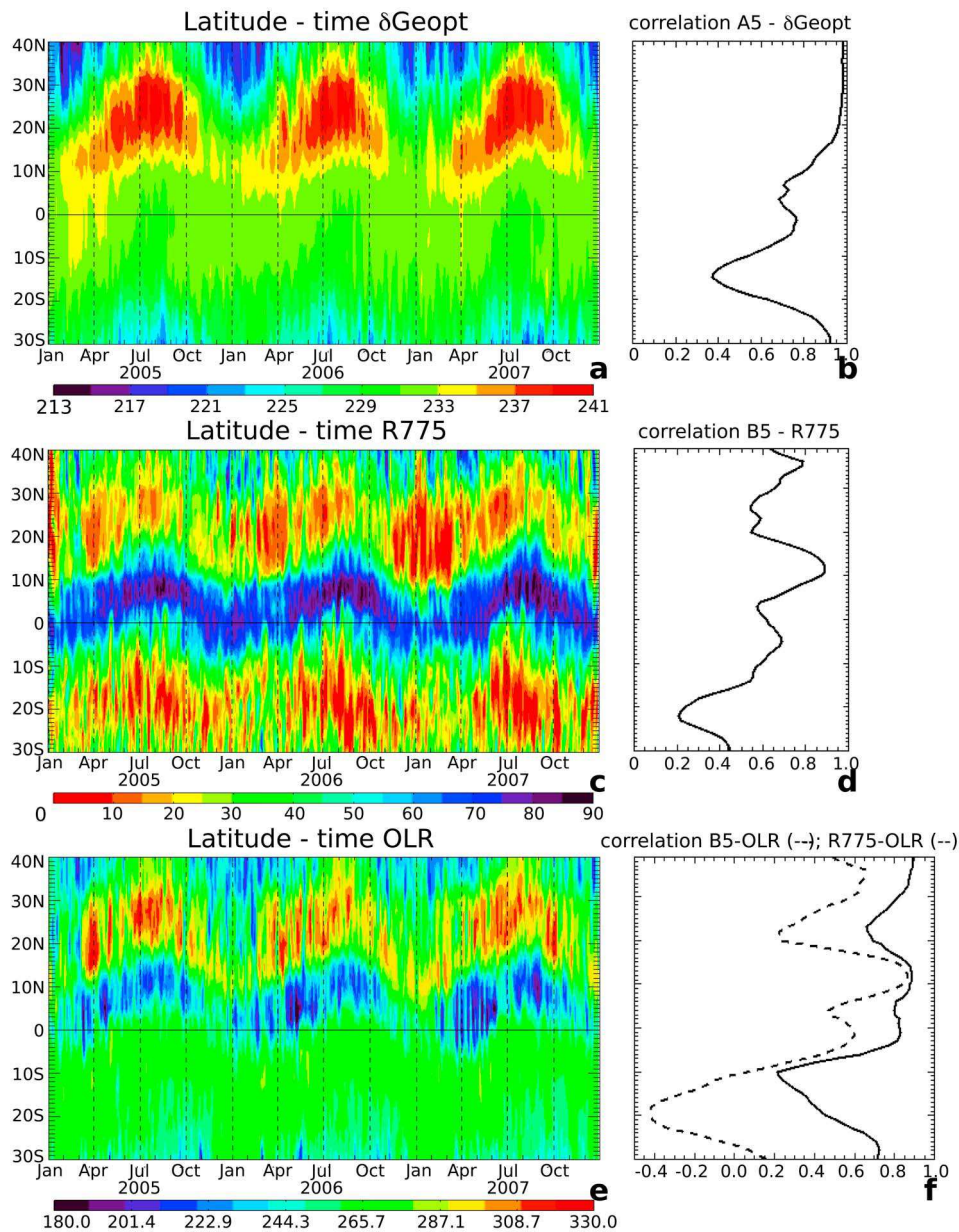
Figure 14. Latitude-time diagrams of ERA-INT (a) geopotential difference (∂Geopt), (c) relative humidity at 775 HPa, (e) OLR for 2005–2007, longitude band 10°W–5°E. A 5 day smoothing was made for the OLR plot. Corresponding correlation coefficients for (b) A5 ∂Geopt, (d) B5-RH775, and (f) B5 (straight line) and -RH775 (dashed line) with OLR. Note that correlations with RH775 are inversed (-RH) to account for the inverse variation sense with respect to B5.

is poorly depicted by RH775 (wide spectral band between 25 to 30 and 50 days). In addition, RH775 exhibits a 12 day mode, which is also found in OLR. It is much lower than the other modes in B5 (observed mainly in January and May 2006, and occasionally at other dates (May 2005, February 2007), in agreement with OLR and RH775.

[42] 3. Gulf of Guinea (10°S–20°S): The 40 day mode dominates in all wavelet series (A5, B5, ERA-INT RH, and ∂Geopt) as seen in the B5 wavelet plot (Figures 16e, 16f, and 17d). At shorter scale, ERA-INT RH shows a 20 day mode (Figure 17d), which is also found in B5 and A5 but for a longer period (25 days). AMSU data (mainly in B5) also

shows a 10–12 day mode, occurring all along the 3 years but which is not obvious when integrating the wavelet spectral energy over the 8 years (imbedded in a wider period up to 20 days). The 40 day mode has a maximal magnitude in March and September 2006 and May 2007 in both B5 and A5, as well as in RH775, but not as well consistent in the ∂Geopt wavelet diagram. On the contrary, the 20–25 day mode variations agree both in ERA-INT and AMSU data, without any seasonal difference (slightly stronger in winter).

[43] In summary, the longest intraseasonal mode (30–40 days) is observed in the monsoon band in AMSU humidity channels (B3 and B5 wavelet diagrams have similar char-
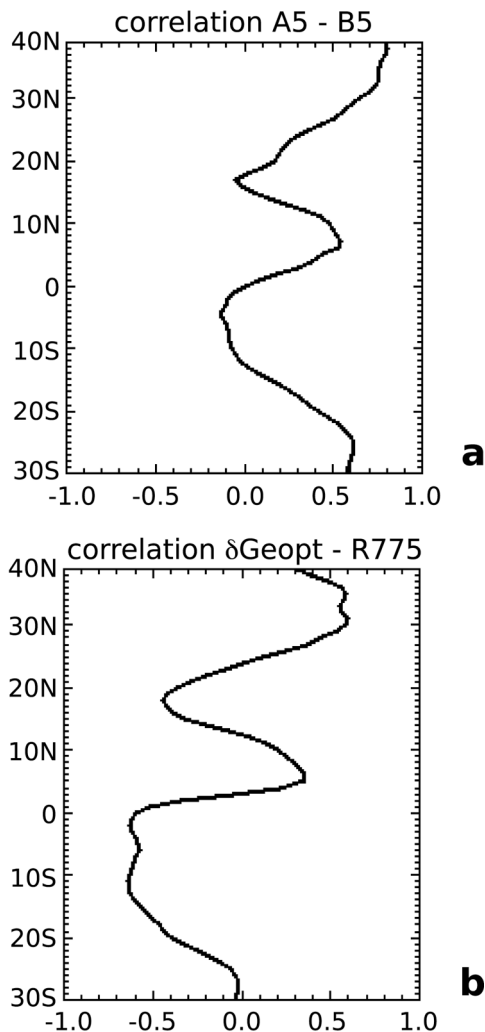
Figure 15. Correlation coefficient of (a) A5 and B5 and (b) ∂Geopt and -RH775.

acteristics). This mode, which also dominates the variability in the Gulf of Guinea and in the HL, may be linked either to the activity of the Madden-Julian Oscillation [*Matthews*, 2004; *Janicot et al.*, 2009] or to the Southern Hemisphere equivalent of the North Atlantic Oscillation [*Foltz and McPhaden*, 2004]. This mode is observed in ERA-INT ∂Geopt in the HL, but is less consistent (longer or shorter period) in the monsoon band and in the Gulf of Guinea. A shorter mode is observed at the three latitudes for periods about 20 days in the monsoon band (AMSU and OLR) and is accompanied by a 10–12 day period mode in the HL and the Gulf of Guinea. The 20 day mode is found in ERA-INT data in the HL and the Gulf of Guinea, but not in the ITCZ, where a shorter period is found.

[44] *Sultan et al.* [2003], *Mounier and Janicot* [2004], and *Mounier et al.* [2008] identified two independent modes of convective activity around 15 days, linked respectively to a westward propagation of the convective envelope over the Sahelian latitudes and to a zonal dipole of convection between the Guinean coast and the mid-Atlantic. Both modes are associated with a modulation of the Sahara heat low activity, especially for the former one (see also

Lavaysse et al. [2009]; *Chauvin et al.* [2010]), the latter being more linked to a modulation of a Walker-type zonal circulation at the equator, which modulates pressure and humidity advection. The corresponding 10–12 day mode in the Gulf of Guinea could also possibly be related to St. Helen's high, whose low wind variations were shown to cool the upper ocean within the equatorial upwelling [*De Coetlogon et al.*, 2010].

[45] Several authors studied shorter modes (3–5 days) associated with the African easterly waves, but the interpolation method used here filters out any period shorter than 6–8 days.

[46] AMSU Tb values can thus be used in complement of OLR to investigate intraseasonal variations. With respect to OLR, AMSU-B features related to deep convection are similar, and differences are due to humidity variations, which are not observed in OLR. AMSU-A channels provide detailed information on temperature variations in dry areas (HL in particular). Both temperature and humidity channels contain variability information relevant for investigating intraseasonal variability in the entire monsoon region. The AMSU data reveals a more complex variability than the one found in model analyses.

4. Summary and Conclusions

[47] This work is in direct line with the AMMA program, which aims to enhance our understanding of the West African monsoon. The objective of this study is to explore the potential of direct use of AMSU-A and -B brightness temperatures, without assimilation or retrieval techniques, to statistically infer the temperature and humidity variability in the atmosphere. AMSU observations are relevant to such diagnostics since they are informative about temperature and humidity at different levels of the atmosphere. However, the use of these observations is not straightforward, and one should take into account the observation zenith angle variability for a proper use of data.

[48] A new statistical technique was used to adjust AMSU-A and -B observations to nadir. Such a correction is necessary since the observation angle variation can potentially introduce variations in observed Tb data, which are much stronger than the natural variations of the observed scene. The limb adjustment method was evaluated: (1) qualitatively by examining monthly mean maps, before and after limb adjusting the data and by analyzing some case studies; and (2) more rigorously by performing radiative transfer simulations. We end up with 8 years of AMSU-A and -B limb-adjusted observations, which were further processed and interpolated to get gridded AMSU images with a one degree grid resolution. In this study only observations from AMSU-A channel 5–7 and from AMSU-B channels 3 and 5 were used.

[49] Comparisons among AMSU data, OLR data, and ERA-INT reanalyses were performed. It is shown that AMSU-A5 data provide the heat content of low atmospheric layers in a similar way as the geopotential difference (700–925 hPa), often used in climate studies. AMSU-B data are found to be highly correlated with the humidity field within the observation layers. Nevertheless, the effect of clouds and rain is obvious in AMSU-B data, as it is the case in OLR data.
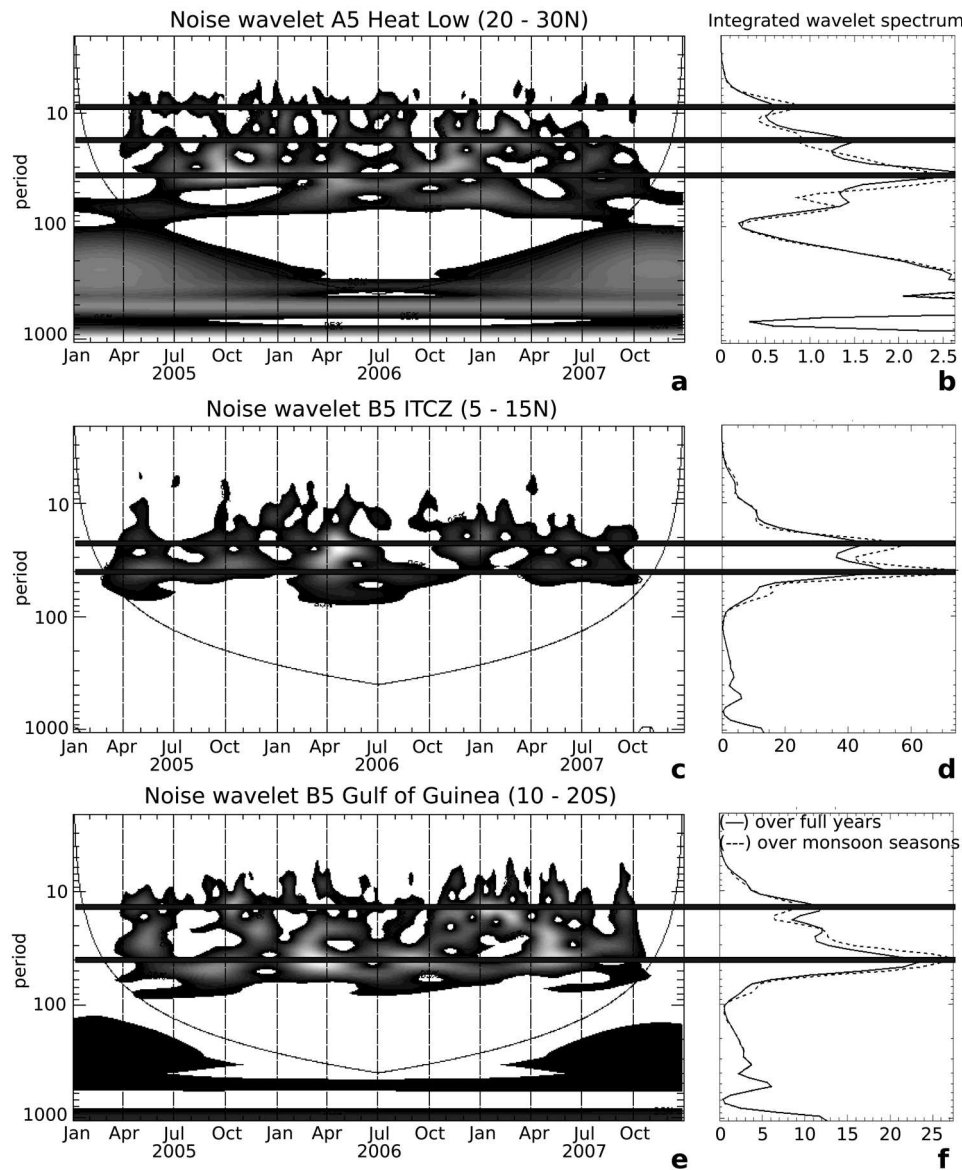
Figure 16. Wavelet spectrum of AMSU data for the years 2005–2007. Plots are for 5°W–5°E, (a, b) 20° N–30°N (A5, heat low), (c, d) 5°–15°N (B5 and monsoon band) and (e, f) 10°S–20°S (B5, Gulf of Guinea). A high-pass filter was applied to remove most effects of the annual cycle. The period (ordinate) is given in days, and spectrum energy is given with a black to white scale. The integrated spectrum is plotted in Figures 16b, 16d, and 16f for the wavelet spectrum in Figures 16a, 16c, and 16e, respectively, over the 3 years (solid line), and over the three monsoon seasons (dashed line). The horizontal lines super-imposed to plots give correspondence between major spectral peaks and wavelets.

[50] It is established that observations from AMSU-A channel 5 can be used to monitor the heat low evolution and that AMSU-B observations from channels 3 and 5 can be used to study the humidity variations in direct link with the African monsoon from intraseasonal to interannual scales. The prominent features are the maximum humidity band associated with the monsoon, as well as the imbedded stronger convective areas and the dry zones associated with the descending branches of the Hadley cells. Comparisons with ERA-INT reanalyses show some similarities but also some differences, as in the maximal latitude of the monsoon band, its overall structure from east to west, and the mag-

nitude and location of the dry areas. Similarities between A5 and ERA-INT geopotential difference are found in the heat low characterization, but the presence of a warmer area in Eastern Africa is also evident from the A5 data, contrary to ERA-INT reanalyses. The weak magnitude of some of these structures (East African dry and hot area, dry area in the Gulf of Guinea) could possibly be related with the too zonal structure of the monsoon band, and its too low maximal latitude in July.

[51] By focusing on the 2005–2007 monsoon periods, it is also shown that the monsoon onset can be depicted from year to year by looking at B3/B5 data, as it is usually done
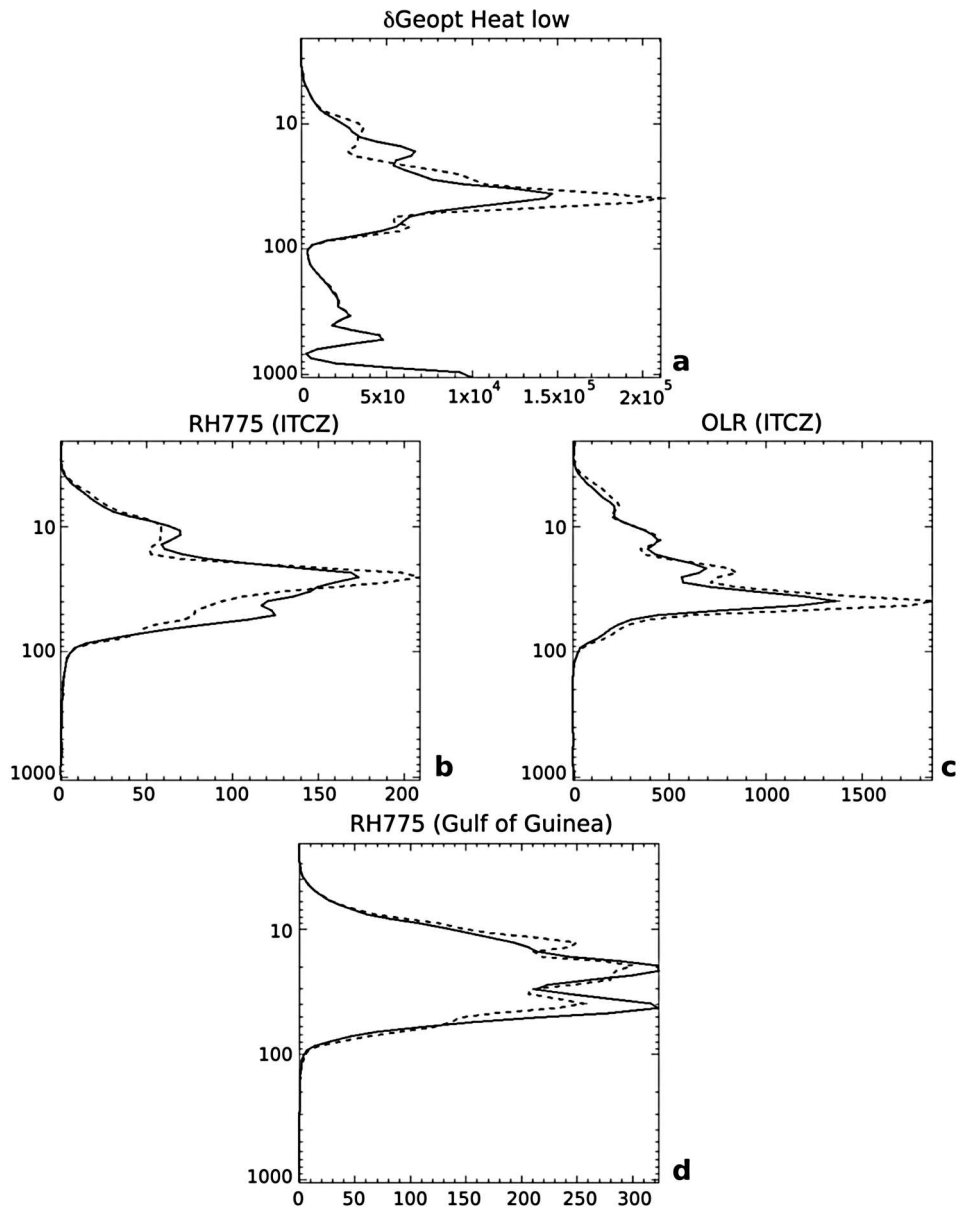
Figure 17. Integrated wavelet spectra of (a) ERA-INT ∂Geopt in the HL, (b) RH775 in the ITCZ, (c) OLR in the ITCZ, and (d) RH775 in the Gulf of Guinea. As in Figure 16, the dashed lines are for integration over the monsoon season (April–September).

using OLR data. Similarly, A5 data properly show the heat low installation in relation with the monsoon onset. Variations from year to year in the date, the spring features of the HL, and the monsoon were observed. Moreover, dry and wet connections between the monsoon band and the mid-latitudes are detected in B3–B5 data. Again, the model humidity does not properly monitor features out of the monsoon band, whereas the geopotential difference is rather well correlated with A5 in the heat low.

[52] Wavelet analysis at various latitudes (in the HL, in the monsoon band, and in the Gulf of Guinea) along the Greenwich Meridian show an intraseasonal variability mode at about 40 days, which is also observed in ERA-INT reanalyses but with a wider range of periods and shorter modes between 10 and 20 days at all three latitudes. The latter modes are not

found in ERA-INT fields in the heat low and Gulf of Guinea. AMSU observations thus confirm previous studies of intraseasonal variability, on the basis of OLR and model analyses, but provide new details on the temperature and humidity variations.

[53] The results presented in this paper are preliminary even if very promising results have been obtained. They show the potential of AMSU data to study the relations between the monsoon variability (onset, intraseasonal variability) and the heat low. These data are very informative about the atmosphere but are still not fully exploited either in meteorological or in climate studies. To further check the reliability of the presented approach, we intend to use Special Sensor Microwave/Imager-Sounder (SSM/I-S) profiler data: thanks to the instrument conical scanning, no

angular correction is needed. It will therefore be possible to fully validate the AMSU data correction method and to estimate its accuracy and limitations.

[54] This study was focusing on the West African monsoon region. By extending the AMSU data processing to the entire tropical band, we will assess the correction method in various climatic zones and evaluate its potential use for tropical climate study.

[55] AMSU data comparison with ERA-INT fields suggest that the model does not reproduce some important features over the African continent and the Gulf of Guinea. This was confirmed for some of them by looking at OLR data. The causes of these discrepancies will be investigated by examining the model analyses in the same area, after assimilation of all AMSU data in clear air [*Karbou et al.*, 2010b].

[56] Finally, we intend to further study the intraseasonal variability over the Gulf of Guinea and the southern tropical Atlantic in connection with the St. Helens anticyclone activity. Similarly, AMSU data appear promising to investigate the heat low activity and its links with moisture advection from its western side (northern Atlantic) and its eastern side (Mediterranean Sea), where in situ data are also very sparse.

References

Agusti-Panareda, A., et al. (2009a), The ECMWF re-analysis for the AMMA observational campaign, *Tech. Memo. 612*, 31 pp, Eur. Cent. for Medium-Range Weather Forecasts, Reading, U. K.

Agusti-Panareda, A., A. Beljaars, C. Cardinali, L. Genkova, and C. Thorncroft (2009b), Impact of assimilating AMMA soundings on ECMWF analyses and forecasts, *Tech. Memo. 601*, 27 pp, Eur. Cent. for Medium-Range Weather Forecasts, Reading, U. K.

Bock, O., et al. (2008), The West African monsoon observed with ground-based GPS receivers during AMMA, *J. Geophys. Res.*, 113, D21105, doi:10.1029/2008JD010327.

Bouchard, A., F. Rabier, V. Guidard, and F. Karbou (2010), Enhancements of satellite data assimilation over Antarctica, *Mon. Weather Rev.*, 138, 2149–2173.

Buehler, S. A., and V. O. John (2005), A simple method to relate microwave radiances to upper tropospheric humidity, *J. Geophys. Res.*, 110, D02110, doi:10.1029/2004JD005111.

Chauvin, F., R. Roehrig, and J. P. Lafore (2010), Intraseasonal variability of the Saharan heat low and its link with midlatitudes, *J. Clim.*, 23, 2544–2561.

Chung, E. S., B. J. Sohn, J. Schmetz, and M. Koenig (2007), Diurnal variation of upper tropospheric activities over tropical Africa, *Atmos. Chem. Phys. Disc.*, 7, 351–381.

Cressman, G. P. (1959), An operational objective analysis system, *Mon. Weather Rev.*, 87, 367–374.

De Coetlogon, G., S. Janicot, and A. Lazar (2010), Intraseasonal variability of the ocean-atmosphere coupling in the Gulf of Guinea during northern spring and summer, *Q. J. R. Meteorol. Soc.*, 136, 426–441, doi:10.1002/qj.554.

Drobinski, P., B. Sultan, and S. Janicot (2005), Role of the Hoggar massif in West African monsoon onset, *Geophys. Res. Lett.*, 32, L01705, doi:10.1029/2004GL020710.

Esbensen, S. K., D. B. Chelton, D. Vickers, and J. Sun (1993), An analysis of errors in special sensor microwave imager evaporation estimates over the global oceans, *J. Geophys. Res.*, 98(C4), 7081–7101.

Eymard, L., C. Klapisz, and R. Bernard (1989), Comparison between Nimbus-7 SMMR and ECMWF model analyses: The problem of the surface latent heat flux, *J. Atmos. Oceanic Technol.*, 6(6), 966–991.

Eyre, J. (1991), A fast radiative transfer model for satellite sounding systems, *Tech. Memo. 176*, 28 pp, Eur. Cent. for Medium-Range Weather Forecasts, Reading, U.K.

Foltz, G. R., and M. J. McPhaden (2004), The 30–70 day oscillations in the tropical Atlantic, *Geophys. Res. Lett.*, 31, L15205, doi:10.1029/2004GL020023.

Goldberg, M. D, D. S. Crosby, and L. Zhou (2001), The limb adjustment of AMSU-A observations: Methodology and validation, *J. Appl. Meteorol.*, 40, 70–83.

Greenwald, T. J., and S. A. Christopher (2002), Effect of cold clouds on satellite measurements near 183 GHz, *J. Geophys. Res.*, 107(D13), 4170, doi:10.1029/2000JD000258.

Guedj, S., F. Karbou, F. Rabier, and A. Bouchard (2010), Toward a better modeling of surface emissivity to improve AMSU data assimilation over Antarctica, *IEEE Trans. Geosci. Remote Sens.*, 48, 1976–1985.

Hong, G., G. Heygster, J. Notholt, and S. A. Buehler (2008), Interannual to diurnal variations in tropical and subtropical deep convective clouds and convective overshooting from seven years of AMSU-B measurements, *J. Clim.*, 21(17), 4168–4189, doi:10.1175/2008JCLI1911.1.

Janicot, S., et al. (2008), Large scale overview of the summer monsoon over West Africa during the AMMA field experiment in 2006, *Ann. Geophys.*, 26, 2569–2595.

Janicot, S., F. Mounier, N. M. Hall, S. Leroux, B. Sultan, and G. Kiladis (2009), The dynamics of the West African monsoon. Part IV: Analysis of 25–90-day variability of convection and the role of the Indian monsoon, *J. Clim.*, 22, 1541–1565.

Jimenez, C., P. Eriksso, V. O. John, and S. A. Buehler (2005), A practical demonstration on AMSU retrieval precision for upper tropospheric humidity by a non-linear multi-channel regression method, *Atmos. Chem. Phys.*, 5, 451–459.

Karbou, F., E. Gérard, and F. Rabier (2006), Microwave land emissivity and skin temperature for amsu-A and -B assimilation over land, *Q. J. R. Meteorol. Soc.*, 620, 2333–2355.

Karbou, F., E. Gérard, and F. Rabier (2010a), Global 4DVAR assimilation and forecast experiments using AMSU observations over land. Part I: Impact of various land surface emissivity parameterizations, *Weather Forecast*, 25, 5–19.

Karbou, F., F. Rabier, J.-P. Lafore, J.-L. Redelsperger, and O. Bock (2010b), Global 4DVAR assimilation and forecast experiments using AMSU observations over land. Part II: Impact of assimilating surface-sensitive channels on the African monsoon during AMMA, *Weather Forecast*, 25, 20–36.

Krzeminski, B., N. Bormann, F. Karbou, and P. Bauer (2008), Towards a better use of amsu over land at ecmwf, paper presented at 16th International TOVS Study Conference, International TOVS Working Group, Angra dos Reis, Brazil.

Lavaysse, C., C. Flamant, S. Janicot, D. Parker, J.-P. Lafore, B. Sultan, and J. Pelon (2009), Seasonal evolution of the West African heat low: A climatological perspective, *Clim. Dyn.*, 33, doi:10.1007/s00382-009-0553-4.

Liebmann, B., and C. A. Smith (1996), Description of a complete (interpolated) outgoing longwave radiation dataset, *Bull. Am. Meteorol. Soc.*, 77, 1275–1277.

Matricardi, M., F. Chevallier, G. Kelly, and J. N. Thépaut (2004), An improved general fast radiative transfer model for the assimilation of radiance observations, *Q. J. R. Meteorol. Soc.*, 130, 153–173.

Matthews, A. J. (2004), Intraseasonal variability over tropical Africa during northern summer, *J. Clim.*, 17, 2427–2440.

Mohr, K. I., and E. J. Zipser (1996), Defining mesoscale convective systems by their 85-GHz ice-scattering signatures, *Bull. Amer. Meteorol. Soc.*, 77, 1179–1189.

Mounier, F., and S. Janicot (2004), Evidence of two independent modes of convection at intraseasonal timescale in the West African summer monsoon, *Geophys. Res. Lett.*, 31, L16116, doi:10.1029/2004GL020665.

Mounier, F., S. Janicot, and G. N. Kiladis (2008), The West African monsoon dynamics. Part III: The quasi-biweekly zonal dipole, *J. Clim.*, 21, 1911–1928.

Prigent, C., F. Chevallier, F. Karbou, P. Bauer, and G. Kelly (2005), AMSU-A surface emissivities for numerical weather prediction assimilation schemes, *J. Appl. Meteorol.*, 44, 416–426.

Ramel, R., H. Gallee, and C. Messager (2006), On the northward shift of the West African monsoon, *Clim. Dyn.*, *26*, 429–440.

Redelsperger, J.-L., et al. (2006a), AMMA: Le projet international d'étude de la mousson Africaine et de ses impacts, *Météorologie*, *54*, 22–32.

Redelsperger, J.-L., C. Thorncroft, A. Diedhiou, T. Lebel, D. Parker, and J. Polcher (2006b), African monsoon multidisciplinary analysis: An international research project and field campaign, *Bull. Am. Meteorol. Soc.*, *87*, 1739–1746.

Roca, R., J.-P. Lafore, C. Piriou, and J.-L. Redelsperger (2005), Extratropical dry air intrusions into the West African monsoon midtroposphere: An important factor for the convective activity over the Sahel, *J. Atmos. Sci.*, *62*(2), 390–407.

Saunders, R. W., M. Matricardi, and P. Brunel (1999), An improved fast radiative transfer model for assimilation of satellite radiance observations, *Q. J. R. Meteorol. Soc.*, *125*, 1407–1425.

Schmetz, J., and O. M. Turpeinen (1988), Estimation of the upper tropospheric relative humidity field from Meteosat water vapor image data, *J. Appl. Meteorol.*, *27*, 889–899.

Simmons, A., S. Uppala, D. Dee, and S. Kobayashi (2007), ERA-Interim: New ECMWF reanalysis products from 1989 onwards, *ECMWF Newsl.*, *110*, 25–35.

Soden, B. J., and F. P. Bretherton (1993), Upper tropospheric relative humidity from the GOES 6.7 μm channel: Method and climatology for July 1987, *J. Geophys. Res.*, *98*(D9), 16,669–16,688.

Spencer, R. W., H. M. Goodman, and R. E. Hood (1989), Precipitation retrieval over land and ocean with the SSM/I: Identification and characterization of the scattering signal, *J. Atmos. Oceanic Technol.*, *6*, 254–273.

Sultan, B., and S. Janicot (2003), The West African monsoon dynamics. Part II: The "preonset" and "onset" of the summer monsoon, *J. Clim.*, *16*, 3389–3406.

Sultan, B., S. Janicot, and A. Dieghou (2003), The West African monsoon dynamics. Part I: Documentation of intraseasonal variability, *J. Clim.*, *16*, 3407–3427.

Ulaby, F. T., R. K. Moore, and A. K. Fung (1981), *Microwave Remote Sensing: Active and Passive*, vol. 1, *Microwave Remote Sensing Fundamentals and Radiometry*, pp 456, Artech House, Norwood, Mass.

Wark, D. Q. (1993), Adjustment of TIROS Operational Vertical Sounder data to a vertical view, *Tech. Rep. NESDIS-64*, 36 pp., Natl. Oceanic and Atmos. Admin., Wash., D. C.

N. Chouaib, L. Eymard, S. Janicot, and F. Pinsard, LOCEAN, IPSL, UPMC/CNRS/IRD/MNHN, Université Pierre et Marie Curie, aile 45-55 4ème étage, Case 100-4 Place Jussieu, F-75252 Paris CEDEX 05, France. (laurence.eymard@locean-ipsl.upmc.fr)

F. Karbou, Météo-France, F-31057 Toulouse, France.